NeuroImage 237 (2021) 118176

Contents lists available at ScienceDirect

NeuroImage

journal homepage: www.elsevier.com/locate/neuroimage

Tractography density affects whole-brain structural architecture and resting-state dynamical modeling

Kyesam Jung[a,b], Simon B. Eickhoff[a,b], Oleksandr V. Popovych[a,b,*]

[a] Institute of Neuroscience and Medicine, Brain and Behavior (INM-7), Research Center Jülich, Germany
[b] Institute for Systems Neuroscience, Medical Faculty, Heinrich Heine University Düsseldorf, Germany

ARTICLE INFO

Keywords:
Structural connectome
Functional connectivity
Kuramoto model
MRI
Whole-brain mathematical modeling

ABSTRACT

Dynamical modeling of the resting-state brain dynamics essentially relies on the empirical neuroimaging data utilized for the model derivation and validation. There is however still no standardized data processing for magnetic resonance imaging pipelines and the structural and functional connectomes involved in the models. In this study, we thus address how the parameters of diffusion-weighted data processing for structural connectivity (SC) can influence the validation results of the whole-brain mathematical models informed by SC. For this, we introduce a set of simulation conditions including the varying number of total streamlines of the whole-brain tractography (WBT) used for extraction of SC, cortical parcellations based on functional and anatomical brain properties and distinct model fitting modalities. The main objective of this study is to explore how the quality of the model validation can vary across the considered simulation conditions. We observed that the graph-theoretical network properties of structural connectome can be affected by varying tractography density and strongly relate to the model performance. We also found that the optimal number of the total streamlines of WBT can vary for different brain atlases. Consequently, we suggest a way how to improve the model performance based on the network properties and the optimal parameter configurations from multiple WBT conditions. Furthermore, the population of subjects can be stratified into subgroups with divergent behaviors induced by the varying WBT density such that different recommendations can be made with respect to the data processing for individual subjects and brain parcellations.

1. Introduction

Some 15 years ago, the human brain connectome was introduced to understand functional brain states which are emerged by structural architecture (Sporns et al., 2005). Over more than a decade, researchers have been investigating the human connectome to elucidate the relationship between structure and function (Goñi et al., 2014; van den Heuvel and Sporns, 2011; Sporns, 2011; Suárez et al., 2020). Recently, network neuroscience provides integrative perspectives to validate biophysically realistic models via structural connectome (Bassett et al., 2018). However, the lack of ground truth and golden standards for the calculation of the human connectome caused a central body of ongoing debates in the literature to validate the macroscopic structural and functional connectivity from neuroimaging data of the human brain (Lindquist, 2020; Maier-Hein et al., 2017; Parkes et al., 2018). In addition, no consensus method has been accepted so far as a standardized approach for calculating the whole-brain connectome (Schilling et al., 2019; Sotiropoulos and Zalesky, 2019). Many studies have investigated the effects of the data processing on the obtained results with respect to reproducibility with different methodologies for structural architecture (Bassett et al., 2011; Buchanan et al., 2014; Cammoun et al., 2012; Dennis et al., 2012; Messaritaki et al., 2019; Owen et al., 2013; Roine et al., 2019), functional homogeneity (Bellec et al., 2015; Thirion et al., 2014), and cortical resolutions for brain modeling (Proix et al., 2016). These studies reported good-to-excellent reliability or stable outcome (Dennis et al., 2012; Owen et al., 2013), recommendation (Messaritaki et al., 2019; Roine et al., 2019), and limitations (Buchanan et al., 2014). At this stage, researchers summarized the influence of data processing for structural brain network measures (Qi et al., 2015). Nevertheless, most of the used techniques, algorithms and parameters for processing the neuroimaging data remain at the level of the best practice lacking a solid theoretical foundation.

Without the ground truth, a model-based approach can be a possible way to investigate the impact of the data processing on the observed brain dynamics and reveal the corresponding mechanisms (Popovych et al., 2019). At this, it is assumed that the considered mathematical models derived from the interactions between brain regions can closely simulate the dynamics of the brain responses. By comparing the simulated and empirical data, we can address the model performance

* Corresponding author.
E-mail addresses: k.jung@fz-juelich.de (K. Jung), s.eickhoff@fz-juelich.de (S.B. Eickhoff), o.popovych@fz-juelich.de (O.V. Popovych).

https://doi.org/10.1016/j.neuroimage.2021.118176.
Received 16 December 2020; Received in revised form 9 May 2021; Accepted 13 May 2021
Available online 15 May 2021.

as given by the results of the model fitting and thoroughly explore the model parameters and dynamics. Consequently, we can apply the model validation to evaluate the data processing by searching for the optimal model parameters that provide the best fitting of the model against the empirical data (Cabral et al., 2011; Endo et al., 2020; Zimmermann et al., 2018). Such an evaluation procedure can be repeated for several modeling conditions, where the parameters of the data processing are varied. In this manner, we can systematically approach the optimal modeling condition and data parameters used for the data processing, which enhances the agreement between the simulated and empirical data.

Previous studies have used different whole-brain tractography (WBT) densities ranging from 5K to 100M tracked streamlines for the human connectome (Bajada et al., 2019; Hagmann et al., 2008; Honey et al., 2009; Prasad et al., 2013; Proix et al., 2016; Roine et al., 2019). In particular, Roine et al. (2019) tested the reproducibility of graph-theoretical measures across varied streamline densities from 10K to 100M and concluded that tractography density should be sufficiently high for excellent reproducibility. High tractography density is also beneficial for highlighting subtle clinical differences, and already 15K-20K streamlines may be sufficient to differentiate between patients with Alzheimer's disease or mild cognitive impairment from healthy controls (Prasad et al., 2013). However, the impact of the WBT density on the human connectome is still unclear. Besides, the derivation of the whole-brain models essentially relies on the underlying network calculated from the whole-brain empirical structural connectivity (SC). The latter provides the brain architecture serving as a backbone for the modeling of brain dynamics (Cabral et al., 2011; Endo et al., 2020; Honey et al., 2009; Zimmermann et al., 2018). It is however difficult to evaluate whether the selected parameters of the data processing for WBT density (e.g., the number of WBT streamlines) are reliably reflecting the brain architecture, and what are the optimal values for modeling, e.g., for maximal similarity between simulated and empirical data. In this study, we address the latter problem and search for the optimal configurations which could lead to the optimal SC extraction resulting in the best fit between the simulated and empirical data.

The broad spectrum of the computational models used for simulation of the brain dynamics ranges from the micro- to the macro-scale (Deco et al., 2008; Endo et al., 2020; Freeman, 1987; Hodgkin and Huxley, 1952; Jansen and Rit, 1995; Wilson and Cowan, 1973). Besides the sophisticated computational modeling concepts, the responses of brain regions can be considered as a harmonized signal (Buzsaki, 2011). Thus, we can also use simple mathematical models of coupled oscillators to generate oscillating brain activity (Breakspear et al., 2010; Kuramoto, 1984; Rodrigues et al., 2016). In particular, systems of coupled phase and generic limit-cycle oscillators were suggested by previous studies for modeling cortical oscillations of the resting-state blood oxygen level-dependent (BOLD) dynamics (Breakspear et al., 2010; Cabral et al., 2011; Deco and Kringelbach, 2016; Deco et al., 2017; Fukushima and Sporns, 2018; Ponce-Alvarez et al., 2015). These studies reported the maximal agreement between simulated and empirical data as given by the Pearson correlation between simulated and empirical functional connectivity (FC) in the range between 0.3 and 0.7. In this study, we consider such a system of coupled phase oscillators to model the slow oscillations of the resting-state BOLD dynamics.

The main topic of the current study is to investigate the impact of the WBT streamline number used for calculation of SC and the average streamline path-length (PL) between brain regions on the simulation results. We considered a system of coupled phase oscillators with delayed coupling (Yeung and Strogatz, 1999), where the anatomical information about brain structural architecture (SC and PL) from diffusion-weighted MRI (dwMRI) was used for its derivation, i.e., to build the model network and approximate the coupling weights and time delay between the network nodes. The latter are the brain regions parceled according to a given brain atlas/brain parcellation. We considered two distinct brain parcellations based on anatomical and functional brain properties. We systematically explored the model parameter space of two free parameters of global coupling and global delay in order to fit the model to empirical data. We also used two model fitting modalities as given by 1) similarity (Pearson correlation) between simulated and empirical FC as a goodness-of-fit of the model and 2) similarity between simulated FC and empirical SC to probe the dynamics of the model as related to its structural network. The obtained simulation results were compared with each other across subjects and simulation conditions, which allowed us to scrutinize the effects of structural architecture modulated by varying WBT density and brain parcellations on the model validation against empirical data. The used approach can also lead to a better understanding of the properties of the obtained data influenced by selected data processing, which can play a key role for the brain modeling as well as data analytics.

2. Materials and methods

The current study considered 351 unrelated subjects (172 males, age 28.5 ± 3.5 years) from the Human Connectome Project (HCP) S1200 dataset (Van Essen et al., 2013). HCP data (https://www.humanconnectome.org) were acquired using protocols approved by the Washington University institutional review board (Mapping the Human Connectome: Structure, Function, and Heritability; IRB #201204036). Informed consent was obtained from subjects. Anonymized data are publicly available from ConnectomeDB (https://db.humanconnectome.org). In the current study, resting-state functional MRI (fMRI), T1-weighted image (T1) and diffusion-weighted images (DWI) from 3T connectome scanners (modified Siemens PRISMA with higher gradient strength) were used for investigation. Resting-state fMRI was acquired with 2 mm isotropic voxels, T1 was in 0.7 mm isotropic voxels, and DWI consisted of 90 directions for 1000, 2000 and 3000 s/mm^2 b-values in total 270 weighted directions with 1.25 mm isotropic voxels.

We reconstructed SC and PL by using six WBT densities and two atlases for individual subjects, then calculated simulated FC from BOLD signals generated by the computational model composed of coupled phase oscillators with delayed coupling. We explored two free parameters of the model for each subject and condition and validated the model through the two model fitting modalities. We also calculated graph-theoretical network properties of SC and PL over considered conditions and compared the network properties with the goodness-of-fit of the model. The individual subjects were stratified into groups based on three criteria derived by the network properties and modeling results. The workflow of the current study is illustrated in Fig. 1.

2.1. Preprocessing of MRI data and connectivity extraction

The current study used an *in-house* pipeline for the extraction of SC and PL matrices from the DWIs. The pipeline consists of four modules: preprocessing of MRI and DWI data, WBT calculation, atlas transformation and connectivity reconstruction. The pipeline is publicly available (https://github.com/inm7/vbc_dwmri). It was optimized for parallel processing on high-performance computational clusters (Jülich Supercomputing Centre, 2018).

The pipeline was created with functions of Freesurfer (Dale et al., 1999), FSL (Smith et al., 2004), ANTs (Tustison et al., 2010), and MRtrix3 (Tournier et al., 2019). Freesurfer was used for processing the T1 including bias-field correction, tissue segmentation, cortical (surface) reconstruction, volume-surface converting, and surface deformation for parcellation as well as for the correction of the eddy-current distortions and head-motion in DWIs using the corresponding b-vectors and b-values. MRtrix3 performed de-noising and bias-field correction on the DWIs. The pre-processed images were used for co-registration between the T1 and the DWIs and linear and non-linear transformation by functions of FSL. Linear and non-linear transformation matrices and images for registration from the standard MNI space to the native space

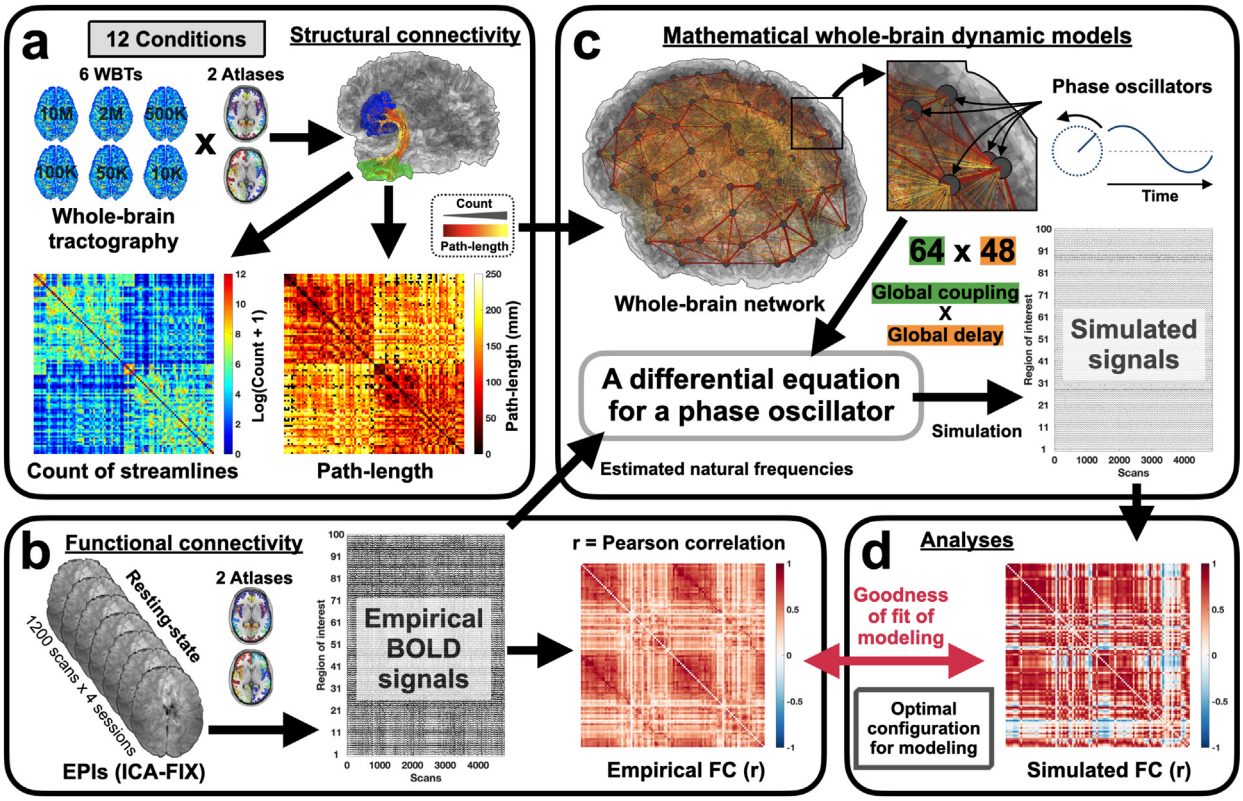

Fig. 1. Workflow of the current study. (a) The whole-brain tractography (WBT) was generated by an in-house pipeline. Structural connectivity (SC) and average path-length (PL) between brain regions were reconstructed based on a given brain parcellation/brain atlas (6 WBTs and 2 atlases). **(b)** The empirical BOLD signals were extracted for each brain region from the ICA-FIX preprocessed HCP data, and the empirical functional connectivity (FC) was calculated between BOLD signals by Pearson correlation coefficient. **(c)** By using the empirical SC and PL matrices, the whole-brain network was reconstructed. The network nodes representing the brain regions were equipped with the phase oscillators (Eq 1) coupled with the coupling weights (Eq 2) and time delays (Eq 3) extracted from the empirical SC and PL matrices, respectively. The natural frequencies of the oscillators were extracted from empirical BOLD signals. The model generated simulated BOLD signals used for the calculation of the simulated FC. **(d)** The simulated FC was compared with empirical FC and SC, and the model was validated by optimizing its parameters for the best correspondence/fitting between the simulated and empirical data. At this, the impact of the data processing on the model validation was evaluated and described.

and vice versa were estimated. Through the image registration, gray matter, white matter, cortical/subcortical, cerebellar and cerebrospinal fluid masks were generated in the native DWI space.

The WBT calculation module included only MRtrix3 functions, where the response functions for spherical deconvolution were estimated using multi-shell-multi-tissue constrained deconvolution algorithm (Jeurissen et al., 2014). Fiber oriented distributions (FOD) were estimated from the DWIs using spherical deconvolution, and the WBT was created through the fiber tracking by the second-order integration over the FOD by a probabilistic algorithm (Tournier et al., 2010). In the latter step, we used six different numbers of total streamlines for varying WBT density: 10K, 50K, 100K, 500K, 2M, and 10M, where the “K” and “M” letters stand for thousand (Kilo-) and million (Mega-), respectively. The tracking parameters were set as default values of *tckgen* function from MRtrix documentation (https://mrtrix.readthedocs.io), where the following values were used: step size = 0.625 mm, angle = 45 degrees, minimal length = 2.5 mm, maximal length = 250 mm, FOD amplitude for terminating tract = 0.06, maximum attempts per seed = 50, maximum number of sampling trials = 1000, and down sampling = 3.

The atlas transformation module applied the linear and non-linear transformation matrix and images to atlases that were sampled in the standard MNI space. We used the Schaefer atlas with 100-area parcellation (Schaefer et al., 2018) and the Harvard-Oxford atlas with 96 cortical regions (Desikan et al., 2006). After the transformation, the labeled voxels in the gray matter mask were selected for a seed and a target region. Consequently, the *tck2connectome* function of MRtrix3 reconstructed SC and PL (count and path-length matrices in Fig 1a).

For the empirical FC, the BOLD signals were extracted from the resting-state fMRI data processed by ICA-FIX as provided by HCP repository (Griffanti et al., 2014). During the ICA-FIX, a weak high-pass filtering (2000 s high-pass filter) was applied for detrending-like effect (Smith et al., 2013). The Schaefer atlas and the Harvard-Oxford atlas were applied for the parcellation of the processed fMRI into brain regions within the standard MNI 2 mm space (6th-generation in FSL). Empirical FC was calculated using Pearson correlation coefficient across BOLD signals extracted as mean signals of the parceled brain regions. There were four resting-state fMRI sessions (1200 volumes, TR = 720 ms) which consist of two different phase-encoding directions (left and right) scanned in different days. In addition, a concatenated BOLD signal was generated by using all four z-scored BOLD signals from the above four fMRI sessions, which resulted in five empirical FCs calculated for BOLD signals from the four fMRI sessions and the concatenated BOLD signals for each subject. Finally, 12 simulation conditions (6 WBTs × 2 atlases) were tested by simulation of the mathematical whole-brain model, where the model parameters were optimized for the best fit between simulated and empirical data.

2.2. Mathematical whole-brain model

We simulated a whole-brain dynamical model of N coupled phase oscillators (Cabral et al., 2011; Kuramoto, 1984; Yeung and Strogatz,

1999)

$$\dot{\varphi}_i(t) = 2\pi f_i + \frac{C}{N}\sum_{j=1}^{N} k_{ij}\sin\left(\varphi_j\left(t-\tau_{ij}\right)-\varphi_i(t)\right)+\eta_i, \quad i = 1,2,\ldots,N. \tag{1}$$

The number of oscillators N corresponds to the number of brain regions parceled as defined by a given brain atlas, where $\varphi_i(t)$ models the phase of the mean BOLD signal of the corresponding region, and the simulated BOLD was calculated as $\sin(\varphi_i(t))$. C is a global coupling which scales the level of couplings of the whole-brain network. η_i is an independent noise perturbing oscillator i, which is sampled from a random uniform distribution from the interval [-0.3,0.3]. The natural frequencies f_i were estimated from the empirical data as frequencies of the maximal spectral peaks (restricted to the frequency range from 0.01 Hz to 0.1 Hz) of the empirical BOLD signals of the corresponding brain regions. k_{ij} stands for the coupling strength between oscillators i and j, and τ_{ij} approximates the time delay of the signal propagation between oscillators i and j. They were calculated from the empirical SC and PL and determined by the following equations:

$$k_{ij} = \frac{w_{ij}}{< W >}, \tag{2}$$

where w_{ij} is the number of streamlines between i^{th} and j^{th} parceled regions and $< W >$ is an averaged number of streamlines over all connections except self-connections, and

$$\tau_{ij} = \frac{L_{ij}}{< V >} = \tau L_{ij}, \tag{3}$$

where τ is a global delay (unit: s/m) which is a reciprocal of an average speed of signal propagation $< V >$ through the whole-brain network. The time step of the numerical integration of Eq 1 by the stochastic Heun method was fixed to 0.04 s, and the simulated signals were generated for 3500 seconds after skipping 500 seconds of the transient. The simulated BOLD signals and the corresponding simulated FCs were calculated from the phases downsampled to TR = 0.72 s, which is the repetition time of HCP fMRI.

The considered mathematical model (Eq 1) has two main free parameters: the global coupling C and the global time delay τ. The global coupling ranged from 0 to 0.504 in evenly discretely distributed 64 values, and the global delay was from 0 to 423 s/m in evenly discretely distributed 48 values. Therefore, 3072 (64 × 48) simulations were performed for each subject to calculate the simulated FCs that were compared with empirical functional and structural data for each simulation condition. A total of 12,939,264 (64 × 48 × 12 × 351) simulations of model (Eq 1) were performed in this study for 351 subjects with 12 conditions (6 WBTs × 2 atlases).

We explored the 2-dimensional model parameter space as mentioned above and found the optimal parameter values for the best correspondence between simulated and empirical data. The correspondence was calculated by Pearson correlation coefficient between simulated FC (sFC) and empirical FC (eFC) and SC (eSC) depending on the model fitting modality. For each subject and simulation condition, 5 parameter planes of the *functional similarity* or *functional model fitting* modality (correlation between sFC and eFC) were obtained corresponding to 5 eFCs. In addition, one parameter plane of the *structure-functional similarity* or *structure-functional model fitting* modality (correlation between sFC and eSC) was also calculated. From each parameter plane, we selected the optimal (C, τ)-parameter point, where the maximal correlation between the simulated and the empirical data was reached. For the functional model fitting the maximal similarity can be referred to as *goodness-of-fit* of the model.

2.3. Effects of different WBT conditions

We revealed the effects of the varying WBT density on the modeling results by evaluating its impact on 1) the graph-theoretical network properties of empirical structural connectome, 2) patterns of the optimal model parameters in the model parameter space, and 3) model performance as given by the quality of the model fitting over simulation conditions. Based on the results from the three approaches, we introduced three criteria (see below) for differentiation of the influence of the WBT density on the modeling results for individual subjects. To do this, we stratified the entire subject population by splitting it into several subgroups according to the mentioned criteria based on *(i)* the relationships between the network properties and the results of the functional model fitting over WBT conditions, *(ii)* distributions of the optimal model parameters of the structure-functional model fitting, and *(iii)* positive and negative slopes (increments) of the goodness-of-fit values (model performance) across the two extreme cases of the considered 10K and 10M WBT streamlines for individual subjects.

2.3.1. Structural architecture and network properties over WBT conditions

To investigate the impact of the varying WBT density on the architecture of structural networks, we calculated graph-theoretical network properties from SC and PL for each subject, WBT condition and atlas. The considered 6 network properties (4 local properties and 2 global properties) included the weighted node degree, clustering coefficient, betweenness centrality, local efficiency, global efficiency and modularity, which were calculated by the brain connectivity toolbox version 2019-03-03 in Matlab (Rubinov and Sporns, 2010). For the local properties, both the average (Avg.) and the standard deviation (S.D.) were calculated.

For every subject, we calculated the Pearson correlation between the values of a given network measure and the maximal functional model fitting (goodness-of-fit) values across varied WBT densities. Then, for every considered network measure, we split the subjects into two subgroups with positive and negative correlations. After that, we performed the two-sample one-tail *t*-test to compare the functional model fitting between the split subgroups. Based on the results of the *t*-test, we selected the network properties, where one of the subgroups showed significantly higher functional model fitting than the other subgroup (Fig. A5 in Supplementary materials). Finally, we overlapped all selected subgroups with higher goodness-of-fit over all selected network properties and referred to this group as pattern 1. Consequently, the rest of subjects were united into the second group referred to as pattern 2. We thus stratified all subjects into two groups/patterns with potentially different impact of the WBT conditions on the modeling results.

2.3.2. Impact of time delay on the model fitting

For another stratification criterion, the optimal model parameters of the maximal correspondence between sFC and eSC were divided into two clusters as suggested by the bimodal distribution splitting small and large values of the optimal time delay (Fig 6). Since subjects can move between the parameter clusters when the total number of the WBT streamlines varies from 10M to 10K, we separated the subjects into five classes: Always staying in cluster 1 (From 1 to 1) or in cluster 2 (From 2 to 2), only once moving either from cluster 1 to cluster 2 (From 1 to 2) or in opposite direction (From 2 to 1), and performing multiple switching between the two clusters (Multiple). This approach based on the distribution of the optimal model parameters was used as the second criterion for stratification of subjects.

2.3.3. Variation of the model performance

The last stratification criterion was based on the behavior of the optimal goodness-of-fit values when the number of WBT streamlines varied. To quantify it, we calculated the increment of the maximal similarity between sFC and eFC matrices of the concatenated session for every individual subject when the number of the WBT streamlines increases from 10K to 10M. Then, all subjects were divided into two subgroups exhibiting either positive or negative slopes (increments) of the goodness-of-fit behavior versus the number of WBT streamlines (Fig 7). According to

Table 1
Sensitivity of the considered graph-theoretical network properties to the variation of the WBT density as revealed by the non-parametric one-way analysis of variance (Kruskal-Wallis ANOVA) test. The corresponding p-values are presented in the right columns of the tables, where the bold p-values indicate that the respective network property significantly changes (Bonferroni corrected $p < .05$) when the number of WBT streamlines varies in the range indicated in the left columns of the tables. The results are shown for the Schaefer atlas (upper table) and the Harvard-Oxford atlas (lower table), and the abbreviations in the upper rows denote the network properties. WD: average weighted node degree, CC: average clustering coefficient, BC: average betweenness centrality, LE: average local efficiency, GE: global efficiency, and MQ: modularity Q.

Schaefer atlas	WD	CC	BC	LE	GE	MQ
10K, 50K, 100K, 500K, 2M, 10M	**<0.001**	**<0.001**	**<0.001**	**<0.001**	**<0.001**	**<0.001**
50K, 100K, 500K, 2M, 10M	**<0.001**	**<0.001**	**<0.001**	**<0.001**	**<0.001**	**<0.001**
100K, 500K, 2M, 10M	**<0.001**	**<0.001**	**0.009**	**<0.001**	**<0.001**	**<0.001**
500K, 2M, 10M	0.994	**<0.001**	0.920	**<0.001**	0.999	**0.011**
2M, 10M	0.916	**<0.001**	0.929	**<0.001**	0.947	1.000
Harvard-Oxford atlas	**WD**	**CC**	**BC**	**LE**	**GE**	**MQ**
10K, 50K, 100K, 500K, 2M, 10M	**<0.001**	**<0.001**	**<0.001**	**<0.001**	**<0.001**	**<0.001**
50K, 100K, 500K, 2M, 10M	**<0.001**	**<0.001**	**<0.001**	**<0.001**	**<0.001**	**<0.001**
100K, 500K, 2M, 10M	0.992	**<0.001**	**0.012**	**<0.001**	1.000	**<0.001**
500K, 2M, 10M	0.996	**<0.001**	1.000	**<0.001**	1.000	**0.005**
2M, 10M	1.000	**<0.001**	1.000	**<0.001**	1.000	0.913

this criterion, the subjects were stratified into two subgroups demonstrating the best functional model fitting for either maximal or minimal number of the WBT streamlines considered. Consequently, we used all three criteria for the three-step stratification analysis (Fig 8).

3. Results

We investigate all three stratification criteria mentioned in the Methods (Section 2.3) and apply them to subject differentiation. This provides an insight into the impact of the WBT density on the model performance for individual subjects and suggests optimal configurations of the data processing parameters. To follow the stratification steps, the obtained results will be presented in parallel for the two considered brain parcellations based on the Schaefer and Harvard-Oxford atlases and compared between them.

3.1. Impacts of WBT density on structural connectome

Figure 2 illustrates the similarities between SC and PL (Fig 2 a and c) and behavior of the weighted node degree, clustering coefficient, betweenness centrality, local and global efficiencies and modularity calculated from the normalized SC matrix over 6 WBT conditions (10K, 50K, 100K, 500K, 2M, and 10M streamlines) for the two atlases (Fig 2 b and d). The similarity of the eSC matrices to the 10M case remains relatively high except for the largest drop at 10K (Fig 2 a1 and c1). On the other hand, the PL matrices have low similarity over the 6 WBT conditions, very quickly deviate from the 10M case, exhibit practically no correlation already for 100K and weakly anti-correlate for 10K (Fig 2 a2 and c2). We also performed a non-parametric one-way analysis of variance (Kruskal-Wallis ANOVA) test over the WBT conditions (Table 1).

By increasing the number of streamlines from 10K to 10M, the number of network edges increases, and the nodes become densely connected, which resulted in monotonically increasing average binarized (discarded weights of edges) node degrees as expected (Fig. A1 in Supplementary materials). However, the weighted node degree based on the normalized count matrices (SC divided by its mean) used in model (Eq 1) shows relatively stationary behavior across the WBT conditions, especially, for dense WBT (Fig 2 b1 and d1 and Table 1 WD). Decreasing the number of streamlines, for example, from 10M to 10K (by 1000 folds) resulted in the corresponding reduction of the averaged weighted node degree of the normalized SC by 6% and 33% for the Schaefer and Harvard-Oxford atlases, respectively (Fig 2 b1 and d1). Similar stationary behavior can also be observed for the average betweenness centrality and the global efficiency, especially, for dense WBT conditions (Fig 2 b3, b5, d3, and d5 and Table 1 BC and GE). The network modularity shows a weak monotonic increase when the WBT density increases (Fig 2 b6 and d6). For these network measures, relatively moderate changes were observed when the number of streamlines varies from 10M to 10K. This indicates that the connectivity in the model is still relatively strong, and some other properties of the network architecture are to a large extent preserved even for the extreme case of 10K WBT.

On the other hand, the average clustering coefficient, local efficiency and their variances strongly decrease when the WBT density increases (Fig 2 b2, b4, d2, and d4 and Table 1 CC and LE). In summary, WBT density modulates the graph-theoretical network properties and results in similar tendencies at the group level through varying WBT density for both atlases. In particular, the clustering coefficient and the local efficiency are significantly different across the WBT conditions already between 2M and 10M cases (Table 1 CC and LE), where very high similarities of SC can be observed (Fig 2 a1 and c1).

3.2. Impacts of WBT density on model fitting

Figure 3 shows the obtained parameter planes and the distributions of the optimal model parameters over all subjects and simulated conditions for the two fitting modalities (sFC versus eFC and sFC versus eSC). The goodness-of-fit between sFC and eFC was observed for small delays for both atlases. This is illustrated in Fig 3 a-d, where the red dots depicting large similarity values are concentrated on the left side of the parameter plane demonstrating, however, different cluster shapes for the Schaefer and the Harvard-Oxford atlases. We also note here that the latter atlas could lead to a stronger fit between the sFC and eFC, compare Fig 3 a and c. In contrast, in the case of the structure-functional model fitting between sFC and eSC (Fig 3 e-h), both atlases demonstrate a similar range of the correspondence (correlation) between simulated and empirical data, however, the maximal similarity can also be attained for large delay.

During the model validation for individual subjects under the 12 considered conditions (6 WBTs × 2 atlases), we also searched for the optimal model parameter, where the maximal similarity between sFC and empirical data (eFC and eSC) was achieved. The distributions of such optimal parameters are depicted in Fig 3 b, d, f, and h for the two fitting modalities and the two brain atlases. In agreement with these results, the best fit between sFC and eFC is attained for small delays (Fig 3 b and d), whereas the strongest structure-function correspondence between sFC and eSC can also be observed for large delays (Fig 3 f and h).

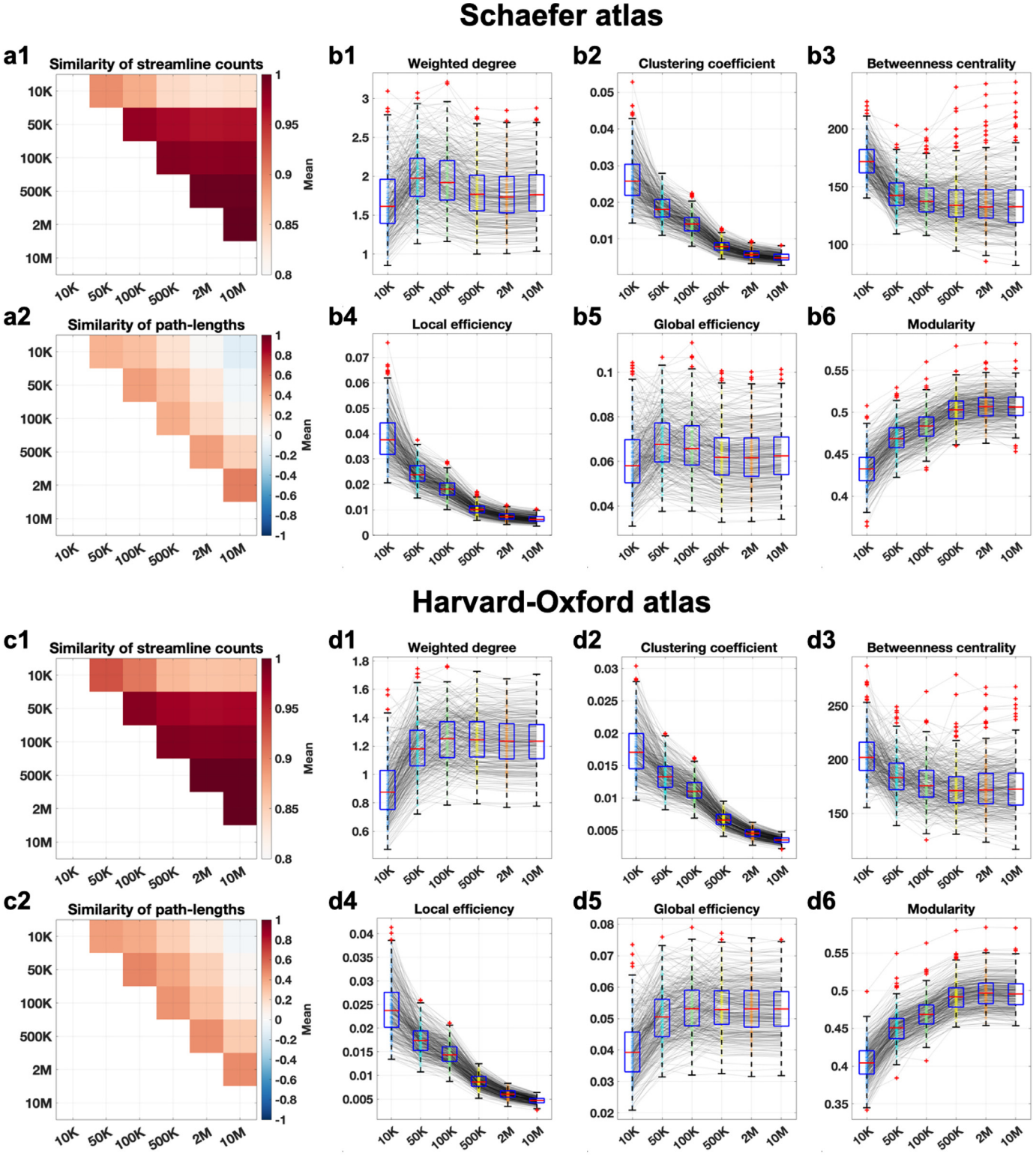

Fig. 2. Impact of the WBT density on the structural architecture. Network measures of the structural connectome and similarity between them calculated for different WBT densities (numbers of streamlines) for **(a, b)** the Schaefer atlas and **(c, d)** the Harvard-Oxford atlas. **(a, c)** Similarity of the connectivity matrices **(a1, c1)** SC and **(a2, c2)** PL calculated for different tractography densities by Pearson correlation across all subjects. **(b, d)** Variations of the network properties calculated from the normalized SC matrix versus WBT density. The plot indices stand for 1: average weighted node degree, 2: average clustering coefficient, 3: average betweenness centrality, 4: average local efficiency, 5: global efficiency, and 6: modularity as indicated in the plot titles. In each plot the thin gray lines depict the behavior of the illustrated quantities for individual subjects together with the box plots, where the red lines, blue boxes and red pluses indicate the medians, the interquartile ranges, and the outliers, respectively. (For interpretation of the references to colour in this figure legend, the reader is referred to the web version of this article.)

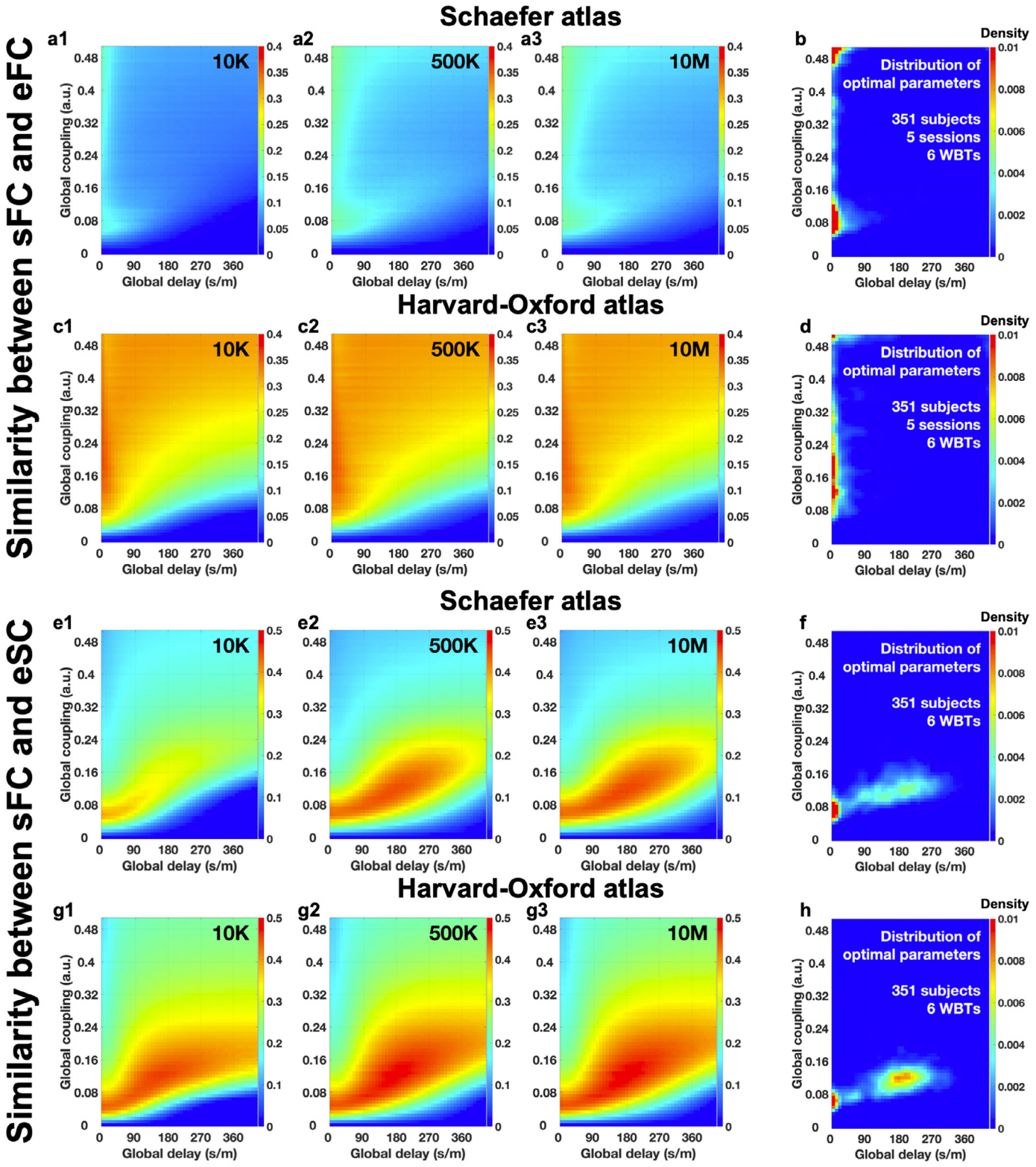

Fig. 3. Parameter planes and the distributions of the optimal model parameters (C, τ) for the two model fitting modalities between simulated and empirical data. Parameter planes are averaged **(1–3)** over all subjects (n = 351) separately for simulation conditions (10K, 500K, and 10M WBT densities) as indicated in the plots (see supplementary Fig. A10 for all conditions). The correspondence between the simulated and empirical data was calculated between **(a-d)** simulated FC and empirical FC and **(e-h)** simulated FC and empirical SC for **(a, b, e, f)** the Schaefer atlas and **(c, d, g, h)** the Harvard-Oxford atlas. The Pearson correlation between the connectivity matrices is depicted by color ranging from small (blue) to large (red) values. **(b, d, f, h)** Distributions of the optimal model parameters of the best model fitting calculated for all individual subjects and simulation conditions. (For interpretation of the references to colour in this figure legend, the reader is referred to the web version of this article.)

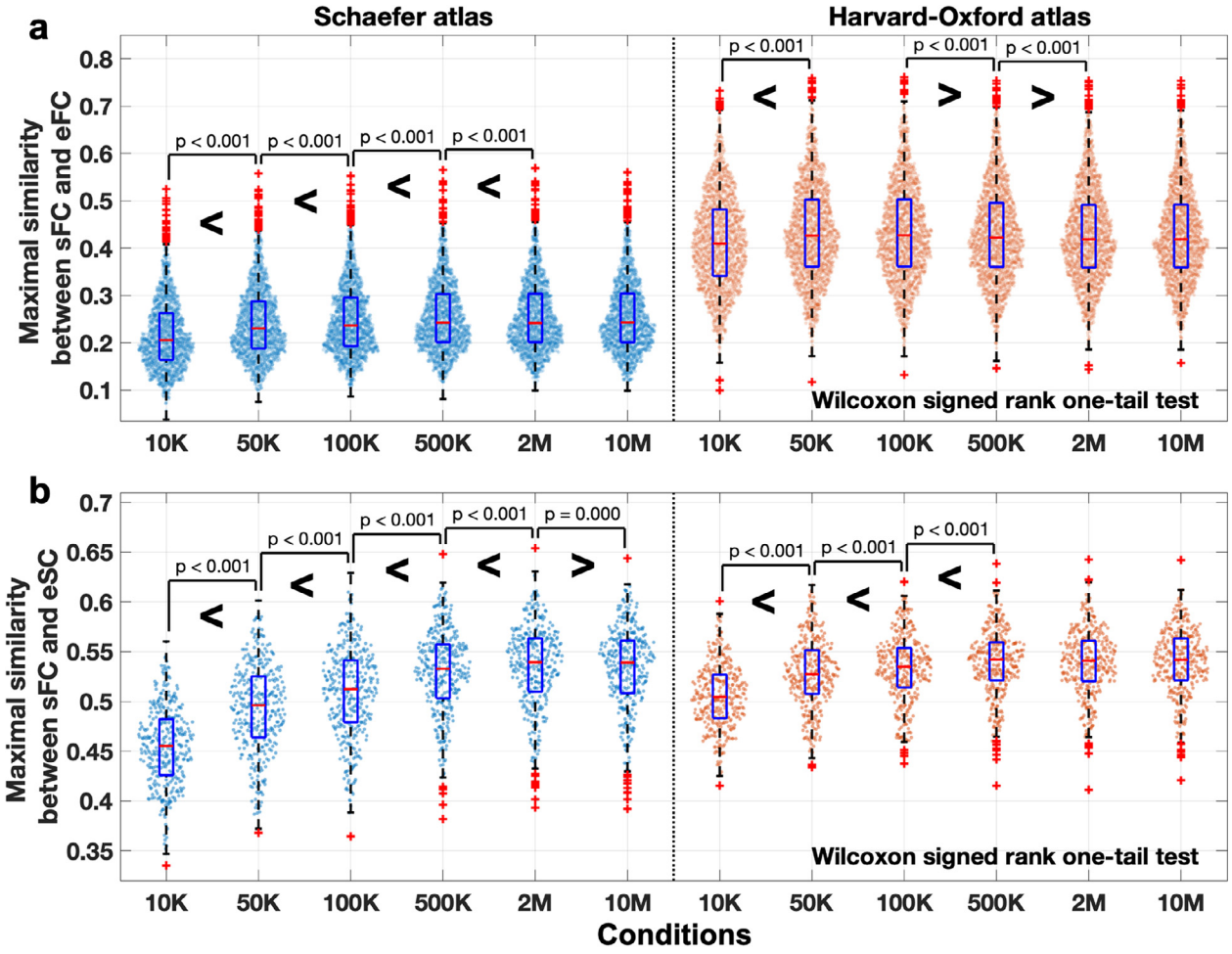

Fig. 4. Results of the model fitting to the empirical data versus 12 simulation conditions (6 WBTs ×2 atlases). The distributions of the maximal similarities for individual subjects between **(a)** simulated FC and empirical FC and **(b)** simulated FC and empirical SC are shown as violin plots for 12 conditions of the WBT streamline numbers indicated on the horizontal axes for the Schaefer atlas (blue violins) and the Harvard-Oxford atlas (orange violins). The results of the pairwise comparisons between the conditions (Wilcoxon signed rank one-tail test) are also indicated with the corresponding p-values in the cases of statistically significant differences (Bonferroni corrected $p < .05$). For the box plots the red lines, blue boxes and red pluses indicate the medians, the interquartile ranges, and the outliers, respectively. (For interpretation of the references to colour in this figure legend, the reader is referred to the web version of this article.)

In the latter case, the parameter distributions apparently demonstrate a two-cluster shape of small and large delays, which is addressed in detail below.

Together with the optimal model parameters for individual subjects, we also collected the corresponding maximal similarities between the simulated and empirical data, which are illustrated in Fig 4 for the 12 simulated conditions and for the two fitting modalities of the correspondence between sFC and eFC (Fig 4a) and between sFC and eSC (Fig 4b). Results of the functional model fitting in all conditions (Fig 4a) were not from the normal distributions, where the null hypothesis was rejected by χ^2 goodness of fit test with $p < .05$. Also in the case of the structure-functional model fitting (Fig 4b) many conditions were not from the normal distributions. Therefore, Kruskal-Wallis test was used for testing significant difference in all conditions (across tractography densities). Consequently, we performed Wilcoxon signed rank one-tail test to evaluate whether the maximal similarities between the simulated and empirical data for one condition are significantly higher or lower than those for the other conditions (see p values in Fig 4).

For the functional model fitting (sFC versus eFC) and the Schaefer atlas (Fig 4a, blue violins), the models with 2M and 10M WBTs performed better than with the other WBTs, and the performance of the model decreased when the number of streamlines decreased. On the other hand, the functional model fitting for the Harvard-Oxford atlas revealed the optimal condition at 50K or 100K WBT (Fig 4a, orange violins). Furthermore, the model could fit better to eFC for the Harvard-Oxford atlas, which was also observed in Fig 3. For the structure-functional model fitting (sFC versus eSC), the situation is different, where 2M or 10M WBTs are preferable for the strongest correspondence between the simulated and empirical data for both atlases demonstrating approximately similar extent of the maximal model fitting (Fig 4b, see also Fig 3).

3.3. *Relationships between network properties and the functional model fitting*

As discussed above, the WBT density modulates the structural connectome. Consequently, it can also influence the dynamics of the model (Figs 3 and 4). In this section, we investigate the effects of the graph-theoretical network properties modulated by WBT density on the model performance.

For each of the considered 6 network properties, we tested the relationships between their values and the maximal similarity between sFC and eFC as given by the Pearson correlation across 6 WBT conditions for each individual subject. The considered network properties demonstrate a pronounced agreement with the goodness-of-fit values at the level of individual subjects (Fig 5 a1 and b1). Some distributions of the correlation coefficients are significantly shifted from zero except

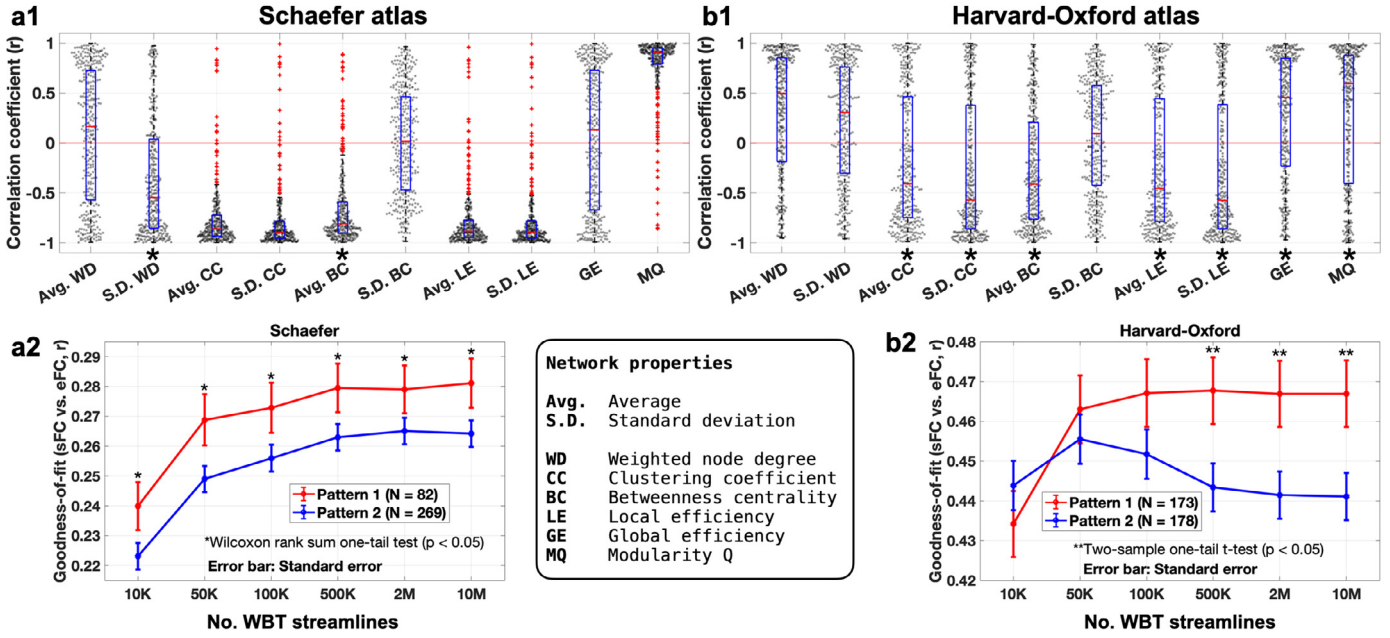

Fig. 5. Relationships between the network properties and the results of the functional model fitting. Correlation between the network properties and maximal similarity between sFC and eFC for individual subjects and fitting results for stratified subjects are shown for **(a)** the Schaefer atlas and **(b)** the Harvard-Oxford atlas. **(a1, b1)** Distributions of the Pearson correlation coefficients calculated across 6 WBT conditions for individual subjects between a given network property indicated on the horizontal axes and the goodness-of-fit values. The gray dots represent the values for individual subjects, and the box plots illustrate the medians (red lines), the interquartile ranges (blue boxes) and the outliers (red pluses). The asterisks on the x-axes indicate statistically significant differences in the goodness-of-fit values between the two subgroups of subjects with positive and negative correlations ($p < .05$ of two-sample one-tail t-test). **(a2, b2)** The results of the functional model fitting versus different numbers of the WBT streamlines for the two subject subgroups of pattern 1 and pattern 2 as indicated in the legends based on the statistically significant split of the subjects for the network properties marked by asterisks in plots a1 and b1, see the Methods Section 2.3.1 for details. The error bars indicate the standard error, and the asterisks denote the simulation conditions, where the pattern 1 and 2 exhibit significantly different extend of the similarity between simulated and empirical data. (For interpretation of the references to colour in this figure legend, the reader is referred to the web version of this article.)

for Avg. WD, S.D. BC, and GE for the Schaefer atlas and S.D. BC for the Harvard-Oxford atlas (see Fig 5 for abbreviations). The presented results are reproducible to retest over individual 5 sessions (4 fMRI sessions and the concatenated case) and merged data of the goodness-of-fit values (see supplementary Fig. A2). Based on the results illustrated in Fig 5 a1 and b1 and supplementary Fig. A2, we can conclude that the changes in the model performance for the individual subjects are related to the changes in the network properties across different WBTs.

The distributions of the correlation coefficients between the network properties and the goodness-of-fit values may differ for different atlases (Fig 5 a1 and b1) indicating a complex relationship between the structural connectome and modeling results. To address such relationships in more detail, we split the subjects into two subgroups of positive or negative correlation for every considered network metric. Then we intersect the groups with highest goodness-of-fit for the network metrics marked by asterisks in Fig 5 a1 and b1 with significant difference between the subgroups and stratify the subjects into two patterns as explained in Methods (Section 2.3.1, see also Figs. A3 - A5 in Supplementary materials).

Based on the results of the tests, for the Schaefer atlas, we selected subjects exhibiting positive correlation with the standard deviation of weighted node degree (S.D. WD+) and negative correlation with the average betweenness centrality (Avg. BC-) for pattern 1, which have significantly higher values of the goodness-of-fit of the model than those of the complementing subgroups (S.D. WD- and Avg. BC+), respectively. The intersection of the two selected subgroups, i.e., S.D. WD+ (n = 93) ∩ Avg. BC- (n = 329) = 82, constituted the stratified pattern 1, whereas the rest of the subjects (n = 269) were grouped into pattern 2.

We found that the two patterns of the split subjects subgroups demonstrate significantly different quality of the goodness-of-fit of the model depending on the WBT conditions (Fig 5a2). For statistical testing of the differences between the patterns 1 and 2, χ^2 goodness of fit test was used to test for a normal distribution for each condition of pattern 1 and pattern 2. The Wilcoxon rank sum one-tail test was then used for a non-parametric test of the difference between the patterns if the null-hypothesis for a normal distribution was rejected by the χ^2 test. Otherwise, two-sample one-tail t-test was used for comparing normal distributions of pattern 1 and pattern 2. The significant differences between the patterns are indicated by asterisks in Fig 5a2, which is the case for any WBT density. We also found that the fitting values for both patterns 1 and 2 monotonically increase for higher WBT density (Fig 5a2). In addition, we tested the changes of the goodness-of-fit of the model for each pattern when the WBT density varies by using Wilcoxon signed rank test. As a result, for the Schaefer atlas, 500K or more streamlines of the pattern 1 and 2M or more streamlines of the pattern 2 showed significantly higher goodness-of-fit values than for any sparser WBT conditions.

For stratification for the Harvard-Oxford atlas, we selected subjects from the intersection of the following subgroups derived as above of positive and negative correlations with the network metrics, which showed significantly higher goodness-of-fit values than the complementing subgroups: Avg. CC-, S.D. CC-, Avg. BC-, Avg. LE-, S.D. LE-, GE+, and MQ+ (see Fig 5 for abbreviations). As above, the sign "+" or "-" after the property name indicates the corresponding subgroups of subjects exhibiting positive or negative correlations with the considered network properties, respectively. Such an intersection of the subgroups resulted in a stratified pattern 1 containing 173 subjects complemented by the others, i.e., 178 subjects of pattern 2.

We here found that patterns 1 and 2 exhibit different behavior of the goodness-of-fit values when the WBT density varies (Fig 5b2). Pattern 1 monotonically increases for large WBT density as before, whereas pattern 2 apparently demonstrates a non-monotonic behavior with an

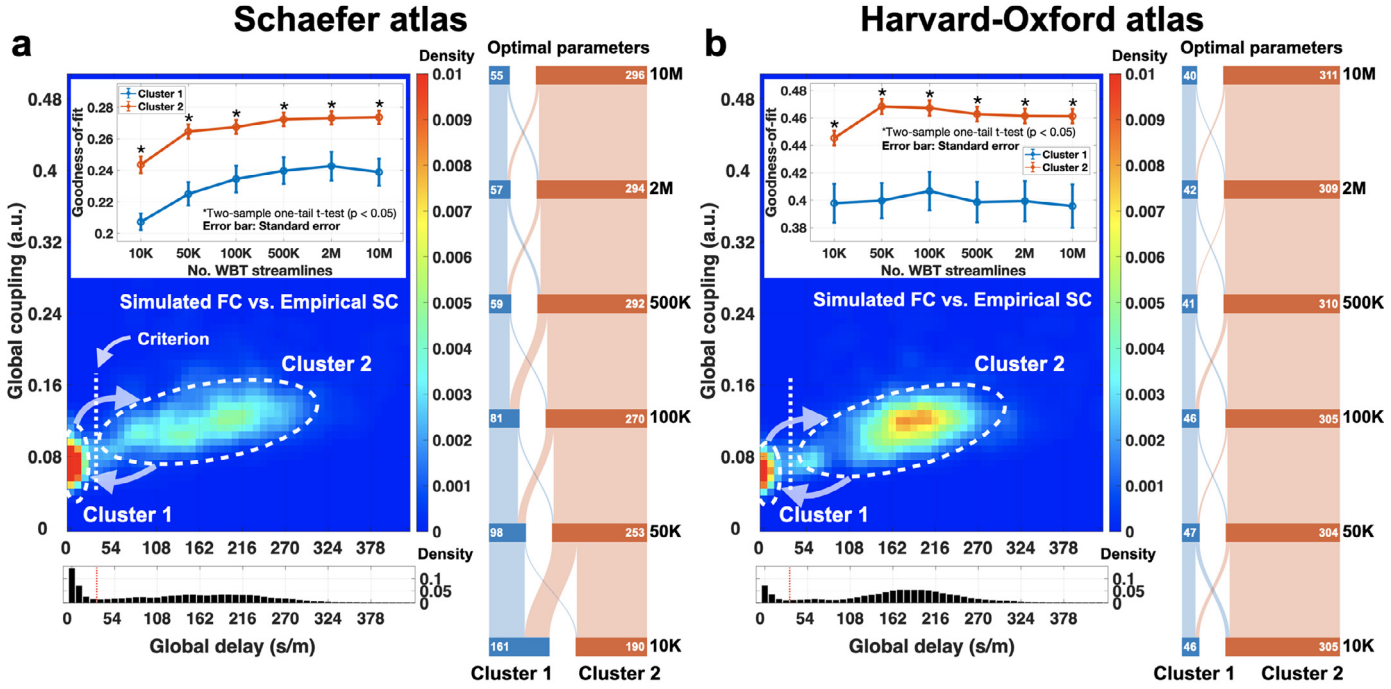

Fig. 6. Clusters of the optimal model parameters of the maximal similarity between simulated FC and empirical SC. The optimal parameters for **(a)** the Schaefer atlas and **(b)** the Harvard-Oxford atlas from Fig 3 f and h, respectively, (n = 2106 values for 351 subjects and 6 WBTs) were split into two subgroups as illustrated in the two lower plots, where the one- and two-dimensional distributions of the optimal parameters are depicted. The upper plots with error bars show the maximal similarity of the functional model fitting between simulated FC and empirical FC of the concatenated fMRI session for the subjects from the two clusters versus the number of the WBT streamlines. The alluvial plots to the right schematically illustrate the interchange of the cluster members when the number of streamlines varies from 10M to 10K. The white numbers in each WBT step indicate the number of subjects in the clusters.

optimal point at 50K of the WBT streamlines. Statistical testing with Wilcoxon signed rank test demonstrated that 100K or more streamlines of pattern 1 showed significantly higher goodness-of-fit values than any sparser WBT condition. However, 50K streamlines of pattern 2 is the optimal condition that shows significantly higher correspondence between the simulated and empirical data than for any other condition, sparser of denser WBT.

Based on the presented results, we can conclude that the optimal number of the WBT streamlines should be considered large (~500K-10M) for the Schaefer atlas (Fig 5a2). Interestingly, the best goodness-of-fit of the model for the Harvard-Oxford atlas can be reached for much sparser WBT at ~50K streamlines for more than 50% of subjects (Fig 5b2).

3.4. *Effects of time delay on model validation*

Based on the clustered distributions of the optimal model parameters of the maximal structure-functional similarity between sFC and eSC (Fig 3 f and h), we divided the optimal parameter points and the corresponding subjects into two clusters (Fig 6). In such a way, the cluster of parameter points with small delay (cluster 1) was split from the other points characterized by relatively large delay (cluster 2) based on their bimodal distributions (Fig 6, the red dotted lines in the histograms in the bottom plots). By dividing the subjects into the two subgroups corresponding to the above clustering of their optimal parameters, we found that the goodness-of-fit values of the functional model fitting are significantly higher in cluster 2 than in cluster 1 consistently for all simulation conditions (all WBTs and both atlases), see Fig 6 (upper plots). Similar effects can also be observed for the structure-functional model fitting between sFC and eSC (see Fig. A6 a2 and b2 in Supplementary materials). The time delay in coupling thus played a constructive role in the model validation against empirical data and led to a better correspondence for structure-functional as well as functional model fitting.

These results also establish a connection between the two fitting modalities and the time delay, where the impact of the latter was not observed in the distributions of the optimal parameters of the functional similarity between sFC and eFC (Fig 3 b and d) and can only be revealed by mediation of the structure-functional correspondence. Another correspondence can be established between the values of the optimal global delays and the natural frequencies of the phase oscillators (Eq 1). To evaluate such a dependence, the broadly distributed positive global delays in cluster 2 were correlated with the mean natural frequencies $\langle f_i \rangle$ averaged over all oscillators (Eq 1). The mean natural frequency of the model is also varying across subjects, and we found a well-pronounced negative correlation between the mean natural frequencies and the optimal delays for the maximal structure-functional similarity between sFC and eSC (see Figs. A7 and A8 in Supplementary materials). This indicates that subjects with slow BOLD oscillations are modeled by system (Eq 1) with large optimal delay if the best correspondence between structure and function has to be achieved.

When the number of the WBT streamlines varies, subjects may exchange their membership in the two clusters (Fig 6, the vertical alluvial plots). Interestingly, for the Schaefer atlas, the ratio of subjects in the two clusters is gradually changing when WBT is getting sparser (from 10M to 10K), where more and more subjects move to cluster 1 approximately balancing the subgroup sizes at 10K case (Fig 6a, the alluvial plot). In contrast, there are only small exchanges of the subjects between clusters for the Harvard-Oxford atlas keeping the group sizes approximately constant for all WBT conditions (Fig 6b, the alluvial plot). Cluster 2 contains most of the subjects as is for both atlases for the case of 10M of the WBT streamlines. We used the splitting of the subjects into the discussed two clusters as the second criterion of the stratification analysis.

It is also important to observe that the structure-functional correspondence between the empirical connectomes eFC and eSC exhibited weak opposite relationships between parameter clusters and across the

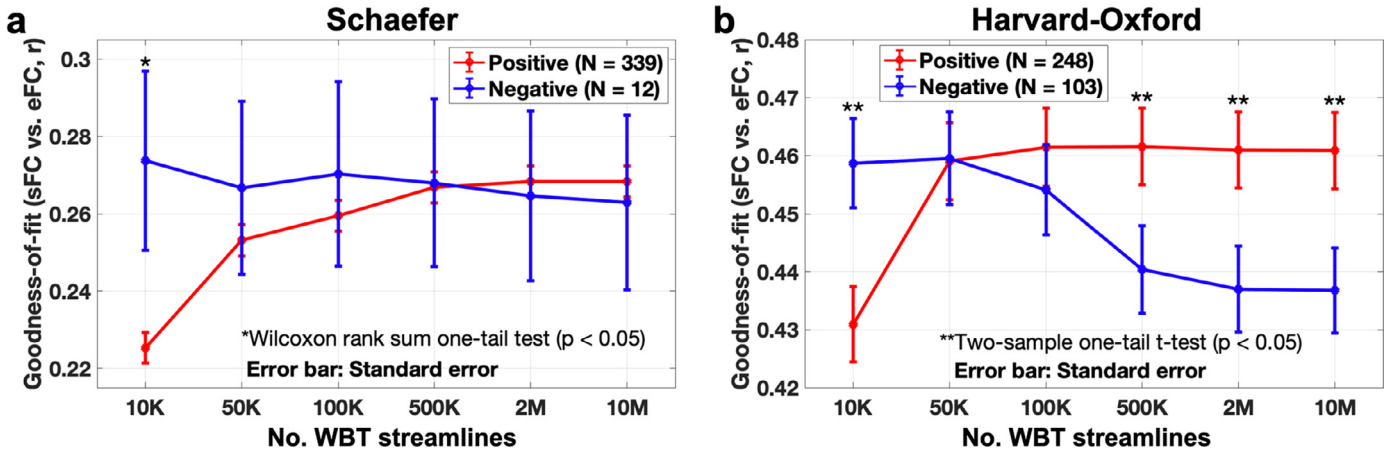

Fig. 7. Subject stratification according to the model performance across 6 WBTs. (a, b) Goodness-of-fit values of the functional correspondence between simulated FC and empirical FC for **(a)** the Schaefer atlas and **(b)** the Harvard-Oxford atlas and for the two groups of the subjects stratified according to the third criterion (see Methods Section 2.3.3). The latter is based on the behavior (positive/negative slopes) of the maximal similarity versus the WBT conditions (see text for details) as indicated in the legends, where the number of subjects in each group is also pointed out. The asterisks indicate the statistically significant differences between the two subject groups ($p < .05$, two-sample one-tail t-test for normal distributions and Wilcoxon rank sum one-tail test for non-parametric test).

number of the WBT streamlines as compared to the correspondence between simulated and empirical data (see Fig. A6 a1 and b1 in Supplementary materials). This indicates a nontrivial character of the reported results that do not directly follow from the empirical structure-function correspondence.

3.5. WBT-Induced changes of model performance

In the previous sections, we observed that the behavior of the goodness-of-fit values versus the WBT conditions is not akin to that of the other atlas. We, therefore, explicitly searched for such divergent dynamics and looked for the subjects with the best model performance for the most sparse or the most dense WBT. The subjects are then split into two subgroups based on the opposite behavior of the model performance when the number of WBT streamlines varies, see Methods (Section 2.3.3) for detail. Figure 7 illustrates the different dynamics of the goodness-of-fit values of the two subgroups of subjects for the two atlases.

As reported before, the maximal similarity between sFC and eFC monotonically increases for the Schaefer atlas when the WBT is getting denser (Figs. 4 - 6). We thus explicitly searched for such conditions, i.e., when the goodness-of-fit was larger for 10M case than for 10K case, and the corresponding line of the model performance had a positive slope. We found that the subjects split very unevenly according to such criterion, and most of them (n = 339) exhibited positive slope, where the similarity between simulated and empirical data monotonically increases when the number of streamlines increases (Fig 7a). Each split subgroup was tested for a normal distribution by χ^2 goodness of fit test over WBT densities. The null hypothesis of the χ^2 test was rejected for each subgroup and each condition. Therefore, we performed Wilcoxon signed rank test. As a result, for the subject subgroup with the positive slope the case of 2M or more WBT streamlines showed significantly higher goodness-of-fit of the model than any sparser WBT condition (Fig 7a, red curve).

In the case of the Harvard-Oxford atlas, the goodness-of-fit values may exhibit a non-monotonic behavior and attained the maximal values at 50K WBTs (Figs. 4 and 5). After stratification according to the third criterion, the both subgroups contain large fractions of the entire subject population with the positive slope (n = 248) and the negative slope (n = 103) (Fig 7b). For the statistic analysis, the null hypothesis of the χ^2 test was not rejected, and we thus performed the two-sample paired t-test. The test resulted in the subgroup with the positive slope showed significantly higher goodness-of-fit of the model with 100K or more WBT streamlines than any sparser WBT condition (Fig 7b, red curve). On the other hand, the subgroup with the negative slope showed significantly higher goodness-of-fit of the model with 50K or less WBT streamlines than any denser WBT condition (Fig 7b, blue curve).

3.6. Stratification analysis

As investigated in the previous sections, the entire subject population can first be split into two groups based on the two patterns of the relationships between network properties and the functional model performance (Fig 5). Second, the subjects can be split based on the clustered distribution of the optimal parameters of the structure-functional maximal similarity between sFC and eSC (Fig 6). Third, different behavior of the goodness-of-fit values of the best correspondence between sFC and eFC can result in positive and negative slopes versus the WBT conditions, which can also be used for subject stratification (Fig 7). By combining all three approaches, we illustrated stratification results in the alluvial plots in Fig 8. Here the proportions of the stratified subjects are shown when the above stratifying criteria are consequently applied to the entire subject population for each atlas. The stratified subjects show different extent and behavior of the goodness-of-fit values of the functional model fitting over the WBT conditions (Fig 8).

In the case of the Schaefer atlas, according to the first criterion, we can expect that subjects of pattern 1 form a relatively small fraction (23%) of the entire subject population, but they have shown higher goodness-of-fit (Fig 5a2 and Fig 8a2). The second stratification step in Fig 8 reflects the interchanging behavior between the parameter clusters observed in Fig 6a. In particular, the stratified group 3 (parameter cluster 2 of large delay) show better performance than the stratified group 2. Finally, the third criterion practically does not differentiate the subjects into positive and negative slopes, see also Fig 7. The declining curves of the goodness-of-fit when the number of the WBT streamlines decreases imply that the optimal number of the total streamlines for the simulation should be considered large, for example, more than 500K: 2M or 10M of the WBT streamlines (Fig 8a2).

For the Harvard-Oxford atlas, subjects stratified into pattern 1 by the first criterion show a monotonic increment of the goodness-of-fit for dense WBT as expected (Fig 8b2, see also Fig 5b2). In addition, we can also expect that the subjects from pattern 2 will have the maximal model performance for sparse WBTs (Fig 5b2 and Fig 8b2). In the second stratification step, the overwhelming majority of subjects from pattern 1 were sorted to the group of persistent members of cluster 2, i.e., the subgroup with large delay for the best structure-functional model fitting

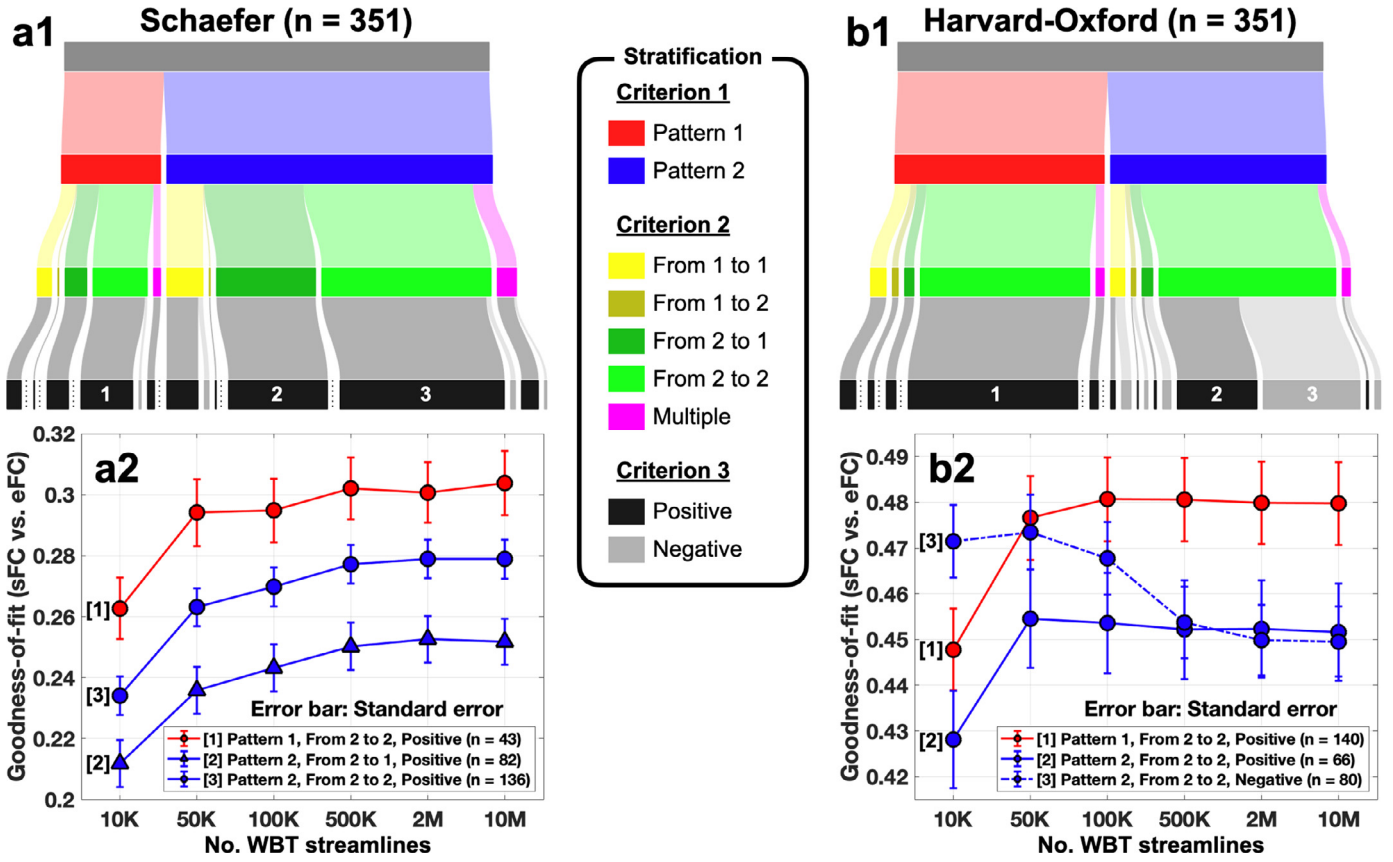

Fig. 8. Stratification analysis with three criteria for two atlases. (a1) The alluvial plot shows all stratified subjects via three criteria and **(a2)** the bottom plot shows goodness-of-fits through 6 WBT conditions for large stratified groups (>35) in the case of the Schaefer atlas. **(b)** The plots by the same analyses for the Harvard-Oxford atlas.

(Fig 8b1, see also Fig 6). Finally, the subjects in pattern 2 can still be split into two subgroups with the inclining and the declining curves of the goodness-of-fit values by the third criterion (Fig 8b2, stratified groups 2 and 3). This can further refine the differentiation of subjects of the best model performance at sparse WBT density (see also Fig 7).

The model evaluation with the Harvard-Oxford atlas shows different optimal conditions than that for the Schaefer atlas (Fig 8b2). The optimal streamline number may depend on the stratification subgroups to which the subject belongs, and which exhibited very different behavior of the goodness-of-fit when the number of streamlines varied (Fig 8b2). For example, the optimal number of streamlines for a better model performance could range from 10M to 100K for the subjects from subgroup 1 in Fig 8b2 (solid red curve). On the other hand, for more than 20% of subjects (n = 80) of the entire subject population, i.e., for those from the stratified group 3 (Fig 8b2, dashed blue curve), the optimal conditions are at ~50K WBT streamlines, and more streamlines may lead to the degradation of the quality of the model validation. For other 18% of subjects (n = 66, group 3 in Fig 8b2, solid blue curve) a sparse WBT can also be a reasonable option.

4. Discussion

The purpose of the current study was to explore how the processing of the neuroimaging data can influence the dynamics and validation of the whole-brain mathematical dynamical models informed by the empirical data. We considered several simulation conditions based on varying data processing parameters, such as the number of total streamlines of WBT and brain atlases. While the latter defined how the brain is parceled into several brain regions that are considered as network nodes in the model, the former influenced the underlying SC (streamline counts) and PL (streamline path lengths) used for the calculation of the coupling weights and time delays in the coupling between nodes. A straightforward interpretation of the investigated number of WBT streamlines as a count of anatomical fiber bundles should be made with caution which was extensively discussed by Jones et al. (2013). Instead, the *reconstructed* streamlines can be considered as a good guess of the white matter connectivity (Caminiti et al., 2013; Jones et al., 2013; Vergani et al., 2014). We discussed how the WBT density can influence the structural information fed to the model and the corresponding modeling results for the considered brain atlases. We found that the parcellation with different atlases showed similar changes of the architecture of the structural networks, but distinct trends of the goodness-of-fit of the model to the empirical data across the number of WBT streamlines. Consequently, we suggested optimal configurations of the considered data and model parameters for the best model fit at the group level as well as for personalized models of individual subjects based on the properties of the empirical and simulated data.

The applied model-based approach followed the line of research suggested and developed in many modeling studies, see, for example, the papers (Breakspear et al., 2010; Cabral et al., 2011; Deco et al., 2017; Fukushima and Sporns, 2018; Honey et al., 2009; Ponce-Alvarez et al., 2015; Popovych et al., 2019) and references therein. The potential of the whole-brain dynamical models to explain the properties of the brain dynamics and structure-function relationship was demonstrated by a detailed investigation of the correspondence between empirical and simulated brain connectomes. At this, the connectivity patterns of the underlying structural network as related to the inter-node coupling strengths and delays can play a crucial role for observing a pronounced structure-function agreement (Popovych et al., 2011; Ton et al., 2014). It is thus important to extract the empirical SC and PL used for evaluation of pa-

rameters of the model connectivity as plausible as possible in order to obtain biologically realistic modeling results (Knock et al., 2009). With this respect, the structure-functional model fitting can be higher than the functional goodness-of-fit as we observed in the current study. One possible explanation might be related to that the empirical SC serves as the underlying backbone of the whole-brain modeling, and simulated FC generated by such models may better replicate the underlying network structure than empirical FC. However, additional investigation is necessary to clarify this question. The current study focuses on the impact of tractography density on the modeling.

4.1. Evaluating structural architecture for modeling

Within the framework of the modeling approach, the model parameters can be varied in a broad range and sense to evaluate their impact on the simulated dynamics. As related to the discussed network topology, beyond the variation of the global coupling strength, the network edges approximating the anatomical connections between brain regions can be removed to obtain a better fit between simulated and empirical FC (Cabral et al., 2012). Aiming at the best correspondence between simulated and empirical data, new inter-region anatomical connections were allowed to be created, or existing structural connections to be rewired according to algorithms based on the differences between the simulated and empirical FC including the gradient-descent method (Deco et al., 2019; 2014). The model connectivity can be composed of both empirical SC extracted from dwMRI data and local intra-cortical connections incorporated into the model based on the distance-dependent approximations (Proix et al., 2016).

Among many possible ways of SC variation for the best model fitting, which might also require additional justifications, we propose to stay within the framework of realistically extracted signals from dwMRI data and consider the well-established approaches for the data processing. In this study, we used state-of-the-art techniques for calculation of WBT and SC (Tournier et al., 2019) and investigated the impact of a constructive parameter for the structural connectome, the number of extracted streamlines on graph-theoretical measures of SC, and their influence on the modeling results.

As discussed in Fig 2 and Table 1, the variation of the WBT density affects the properties of the model networks calculated from the structural connectome, especially, the PL matrices, where the edges with relatively small numbers of streamlines are sensitive to reducing the total number of tracking trials. Therefore, SC extracted from relatively sparse WBT with small number of streamlines may not guarantee a higher reproducibility with stable network properties, where some edges will be disconnected or reconnected from time-to-time, when streamlines will be generated. We, nevertheless, considered an extreme case of 10K WBT streamlines in this study to illustrate the effects observed for very sparse WBT density.

4.2. Graph-theoretical network properties across conditions

For the extraction of the brain structural and functional connectomes and for setting up the model network, we used two paradigmatically distinct brain atlases. These are the Schaefer atlas (Schaefer et al., 2018) that is based on functional MRI data, and the Harvard-Oxford atlas of anatomy-related parcellation (Desikan et al., 2006) that is based on the landscape of gyri and sulci on the cortical surface. We found that the graph-theoretical properties of the structural networks built based on these two parcellations are changing with similar tendencies across the considered WBT conditions for both atlases (Fig 2 and Table 1).

Some of the considered network properties exhibit high sensitivity to the variations of the WBT density, for example, the clustering coefficient (CC) or the local efficiency (LE), see Table 1. On the other hand, the weighted node degree (WD) or the global efficiency (GE) manifested significant changes only when the number of the calculated WBT streamlines was decreased from 10M to 100K or 50K, i.e., 100–200 times. The sensitivity was stronger for the Schaefer atlas. These findings might be of importance when the discussed network properties influence the modeling results. We also found that the mentioned network metrics (CC and LE) with sensitive dependence on the WBT density strongly anti-correlate with the goodness-of-fit of the model for the Schaefer atlas (Fig 5a1), while the dependence is weak with insensitive network measures (WD and GE). Given the impact of the WBT density on the properties of the structural networks (Fig 2), this may explain the clear monotonic behavior of the goodness-of-fit for the Schaefer atlas versus the number of streamlines (Fig 5a2). The situation is different for the Harvard-Oxford atlas, where the relationship with CC and LE is in average less pronounced, whereas the correlation with WD and GE is more enhanced (Fig 5b1). This may explain the apparently mixed behavior of the goodness-of-fit for this brain atlas (Fig 5b2).

In summary, some of the network metrics are characterized by different relationships with the results of the model validation for the varying WBT density for different parcellations, see also supplementary Figs. A3 and A4 for the relationships of all considered network properties. Therefore, even if the tractography density modulates the graph-theoretical network properties in similar changes for the considered atlases as we observed, it can however influence the dynamics of mathematical models in different ways depending on the used brain parcellation.

4.3. Role of time delay in the modeling

It is interesting to note here that the best agreement between simulated and empirical functional data (sFC and eFC) was attained for the considered model at small (zero) delays (Fig 3). It is therefore safe to consider such a type of model simulating ultra slow BOLD dynamics without delay in coupling (Deco et al., 2019; 2017; Ponce-Alvarez et al., 2015). Nevertheless, the goodness-of-fit for the model with delay (including zero delay) exhibits around 9% larger values than that without delay (zero delay only), see Fig. A9 a and b in Supplementary materials. On the other hand, the role of delay in coupling is apparent for the structure-functional (sFC-eSC) model fitting, where the correspondence between sFC and eSC is also enhanced by around 14% for the model with delay when compared to the case without delay (Fig. A9 c and d in Supplementary materials).

We also reported on the clustered distributions of the optimal model parameters for the structure-functional model fitting sFC-eSC and their behavior (migration between clusters) when the WBT density varies for the two considered brain atlases (Fig 6). Such a behavior of the optimal parameters might be related to the performance of the model at the group level. Indeed, we observed that subjects from the parameter cluster with large delay demonstrated better quality of the model validation for both functional and structure-functional model fittings (Fig 6 and supplementary Fig. A6). In other words, if the optimal parameters for the maximal sFC-eSC correspondence have a large delay, we might expect a better correspondence between sFC and eFC. Accordingly, we might also expect that the group-averaged goodness-of-fit for the Schaefer atlas will decay faster than that for the Harvard-Oxford atlas when the number of streamlines decreases as observed in Fig 4. This is because parameter points (subjects) migrate to the cluster with small delay, and fewer optimal parameter points with large delay can be found for a sparser WBT for the Schaefer atlas. These arguments can suggest a possible mechanism associated with the impact of time delay in coupling on the model fitting results.

The values of the optimal non-zero delays for the structure-functional fitting modality can be influenced by the natural frequencies of oscillators (Eq 1) demonstrating relatively strong negative correlations with the structure-functional model fitting as illustrated in supplementary Figs. A7 and A8. Therefore, the average frequency of BOLD oscillation for a given subject can influence the values of the optimal delay for the best structure-functional correspondence. The parameter of the global delay scales the average velocity of signal propagation between brain regions. Consequently, the optimal speed of the signal propagation in the

brain as revealed by the modeling results can be regulated by the mean intrinsic time scale of oscillatory activity of individual brain regions.

4.4. Stratification analysis and optimal conditions

The problem of the optimal number of the total WBT streamlines was also addressed in this study beyond the group-level analysis and aimed at the best fitting of the personalized models for individual subjects. To investigate the impact of the WBT density at the level of individual subjects, we stratified the entire subject population into smaller subgroups with more homogeneous (heterogeneous) model dynamics within (between) subgroups. One of the stratification approaches is to show the effect of the graph-theoretical network properties modulated by the WBT density on performance of the model. We found that such correlations for individual subjects are well-pronounced for the Schaefer atlas, but they are somewhat less expressed for the Harvard-Oxford atlas (Fig 5 a1 and b1). Nevertheless, the stratification can be designed by combining the splitting results for different network properties, which resulted in a clear differentiation of the impact of the WBT streamline number on the model validation across stratified subgroups and brain parcellations (Fig 5).

Another approach to stratification of the subjects was based on the clustering of the optimal delay for the structure-functional model fitting discussed above. It can provide an informed view on the validation results for the functional model fitting (Fig 6). One more stratification approach is illustrated in Fig 7, where the subjects were split into two subgroups of qualitatively different individual behavior of the goodness-of-fit versus the streamline number. Based on the obtained results, we can propose to use the large number (~2M-10M) of the WBT streamlines for the best functional model validation, if the Schaefer atlas was used for the brain parcellation.

On the other hand, the recommendation is completely opposite for more than 20% of subjects for the brain parcellation based on the Harvard-Oxford atlas (Fig 8b2, blue dashed curve 3). For such subjects, the large number of streamlines can lead to a lower quality of the model fitting as compared to rather sparse WBT containing, for example, only 50K streamlines. Differentiating the subjects according to the discussed stratification criteria can help to design an individual data processing workflow and configurations of parameters for the optimal personalized modeling of the brain dynamics. In particular, based on the obtained results, we can suggest a personalized optimal number of the WBT streamlines for the considered brain parcellation for the better model performance at the modeling of the resting-state brain dynamics.

Based on the results of the stratification analysis, we may suggest a few tentative guidelines to possible evaluation of personalized optimal number of the WBT streamlines for the whole-brain model of the resting-state brain dynamics.

- Around 50K WBT streamlines can be considered as a sparse WBT condition.
- More than 2M WBT streamlines can be considered as a dense WBT condition.
- Graph-theoretical network properties of the structural connectome can influence the goodness-of-fit of the model over different tractography densities. Such relationships to the data variables may contribute to the mechanism of the fitting variability and subject stratification into qualitatively different subgroups.
- Modeling with time delay in coupling can enhance goodness-of-fit of the model.
- A dense WBT is not always the best condition for the whole-brain modeling.
- Brain parcellation may affect the optimal parameters of the data processing and should be taken into account already at early stages of the data analytics.

To understand the underlying mechanism of the stratification results, more detailed investigation aimed at quantitative validations and generalization of the results should be performed. From the results of the current study we can already conclude that optimal configurations of the data processing and quantitative guidelines are important for personalized data processing and modeling.

4.5. Limitations and future direction

Although we used the data with high quality of the data preprocessing and physiological noise reduction, however, we note that the reported results were obtained from the neuroimaging data of young adults with relatively narrow age ranges. In order to generalize our conclusions, they have to be verified for other datasets with broader distribution of the phenotypic parameters and other data quality such as clinical-grade scans.

The current study used empirical FC based on the resting-state fMRI measurements for evaluation of the model performance. Regarding other data modalities, future works can include electrophysiological data with electrical modeling for general outcomes. Furthermore, other fitting modalities can also be possible metrics to evaluate whole-brain modeling, for instance, dynamic FC or effective connectivity. Detailed investigation under such conditions can contribute to a better coverage and optimization of the model validation for personalized modeling.

5. Summary and conclusion

We found that varying number of total streamlines for WBT affects the network properties of the structural connectome and performance of the mathematical modeling of the resting-state brain dynamics. The results showed that a dense WBT is not always the best condition for the whole-brain mathematical modeling represented by a system of interacting oscillators with time delay in coupling. We also demonstrated that the optimal parameters of the data processing may be affected by the utilized brain parcellation that should be taken into account already at early steps of the data processing workflow. The present study did not aim to provide any quantitative conclusion concerning the optimal number of WBT streamlines, but rather to illustrate possible qualitative effects caused by the varying WBT density on the structural connectome and modeling results in combination with functional and anatomical brain parcellations. Our results can contribute to a better understanding of the interplay between the data processing and model parameters and their influence on data analytics of dwMRI and modeling of the resting-state fMRI data.

Data and Code Availability Statement

Anonymized data are publicly available from ConnectomeDB (https://db.humanconnectome.org).

The structural connectivity pipeline is available from GitHub (https://github.com/inm7/vbc_dwmri).

Declaration of Competing Interest

The authors have declared that no competing interests exist.

Credit authorship contribution statement

Kyesam Jung: Conceptualization, Data curation, Formal analysis, Investigation, Methodology, Software, Validation, Visualization, Writing - original draft, Writing - review & editing. **Simon B. Eickhoff:** Conceptualization, Funding acquisition, Resources, Writing - review & editing. **Oleksandr V. Popovych:** Conceptualization, Data curation, Funding acquisition, Methodology, Project administration, Resources, Software, Supervision, Validation, Writing - review & editing.

Acknowlgedgments

The authors are grateful to Esther Florin for fruitful discussions, helpful comments on the manuscript and advices concerning statistical analysis. The authors gratefully acknowledge the computing time granted through JARA on the supercomputer JURECA at Forschungszentrum Jülich. This work was supported by the Portfolio Theme Supercomputing and Modeling for the Human Brain by the Helmholtz association (https://www.helmholtz.de/en), the Human Brain Project, and the European Union's Horizon 2020 Research and Innovation Programme (https://cordis.europa.eu) under Grant Agreements 720270 (HBP SGA1), 785907 (HBP SGA2), 945539 (HBP SGA3), and 826421 (VirtualBrainCloud). The funders had no role in study design, data collection and analysis, decision to publish, or preparation of the manuscript.

Data were provided S1200 by the Human Connectome Project, WU-Minn Consortium (Principal Investigators: David Van Essen and Kamil Ugurbil; 1U54MH091657) funded by the 16 NIH Institutes and Centers that support the NIH Blueprint for Neuroscience Research; and by the McDonnell Center for Systems Neuroscience at Washington University.

Supplementary material

Supplementary material associated with this article can be found, in the online version, at 10.1016/j.neuroimage.2021.118176

References

Bajada, C.J., Schreiber, J., Caspers, S., 2019. Fiber length profiling: a novel approach to structural brain organization. Neuroimage 186, 164–173. doi:10.1016/j.neuroimage.2018.10.070.

Bassett, D.S., Brown, J.A., Deshpande, V., Carlson, J.M., Grafton, S.T., 2011. Conserved and variable architecture of human white matter connectivity. Neuroimage 54 (2), 1262–1279. doi:10.1016/j.neuroimage.2010.09.006.

Bassett, D.S., Zurn, P., Gold, J.I., 2018. On the nature and use of models in network neuroscience. Nat. Rev. Neurosci. 19 (9), 566–578. doi:10.1038/s41583-018-0038-8.

Bellec, P., Benhajali, Y., Carbonell, F., Dansereau, C., Albouy, G., Pelland, M., Craddock, C., Collignon, O., Doyon, J., Stip, E., Orban, P., 2015. Impact of the resolution of brain parcels on connectome-wide association studies in fmri. Neuroimage 123, 212–228. doi:10.1016/j.neuroimage.2015.07.071.

Breakspear, M., Heitmann, S., Daffertshofer, A., 2010. Generative models of cortical oscillations: neurobiological implications of the kuramoto model. Front. Hum. Neurosci. 4. doi:10.3389/fnhum.2010.00190.

Buchanan, C.R., Pernet, C.R., Gorgolewski, K.J., Storkey, A.J., Bastin, M.E., 2014. Test–retest reliability of structural brain networks from diffusion mri. Neuroimage 86, 231–243. doi:10.1016/j.neuroimage.2013.09.054.

Buzsaki, G., 2011. Rhythms of the brain. Cary: Oxford University Press doi:10.1093/acprof:oso/9780195301069.001.0001.

Cabral, J., Hugues, E., Kringelbach, M.L., Deco, G., 2012. Modeling the outcome of structural disconnection on resting-state functional connectivity. Neuroimage 62 (3), 1342—1353. doi:10.1016/j.neuroimage.2012.06.007.

Cabral, J., Hugues, E., Sporns, O., Deco, G., 2011. Role of local network oscillations in resting-state functional connectivity. Neuroimage 57 (1), 130–139. doi:10.1016/j.neuroimage.2011.04.010.

Caminiti, R., Carducci, F., Piervincenzi, C., Battaglia-Mayer, A., Confalone, G., Visco-Comandini, F., Pantano, P., Innocenti, G., 2013. Diameter, length, speed, and conduction delay of callosal axons in macaque monkeys and humans: comparing data from histology and magnetic resonance imaging diffusion tractography. J. Neurosci. 33 (36), 14501–14511. doi:10.1523/JNEUROSCI.0761-13.2013.

Cammoun, L., Gigandet, X., Meskaldji, D., Thiran, J.P., Sporns, O., Do, K.Q., Maeder, P., Meuli, R., Hagmann, P., 2012. Mapping the human connectome at multiple scales with diffusion spectrum mri. J. Neurosci. Methods 203 (2), 386–397. doi:10.1016/j.jneumeth.2011.09.031.

Dale, A.M., Fischl, B., Sereno, M.I., 1999. Cortical surface-based analysis: i. segmentation and surface reconstruction. Neuroimage 9 (2), 179–194. doi:10.1006/nimg.1998.0395.

Deco, G., Cruzat, J., Cabral, J., Tagliazucchi, E., Laufs, H., Logothetis, N.K., Kringelbach, M.L., 2019. Awakening: predicting external stimulation to force transitions between different brain states. PNAS; Proceedings of the National Academy of Sciences 116 (36), 18088–18097. doi:10.1073/pnas.1905534116.

Deco, G., Jirsa, V.K., Robinson, P.A., Breakspear, M., Friston, K., 2008. The dynamic brain: from spiking neurons to neural masses and cortical fields. PLoS Comput. Biol. 4 (8), e1000092. doi:10.1371/journal.pcbi.1000092.

Deco, G., Kringelbach, M.L., 2016. Metastability and coherence: extending the communication through coherence hypothesis using a whole-brain computational perspective. Trends Neurosci. 39 (3), 125–135. doi:10.1016/j.tins.2016.01.001.

Deco, G., Kringelbach, M.L., Jirsa, V.K., Ritter, P., 2017. The dynamics of resting fluctuations in the brain: metastability and its dynamical cortical core. Sci. Rep. 7 (1). doi:10.1038/s41598-017-03073-5.

Deco, G., McIntosh, A.R., Shen, K., Hutchison, R.M., Menon, R.S., Everling, S., Hagmann, P., Jirsa, V.K., 2014. Identification of optimal structural connectivity using functional connectivity and neural modeling. J. Neurosci. 34 (23), 7910—7916. doi:10.1523/JNEUROSCI.4423-13.2014.

Dennis, E.L., Jahanshad, N., Toga, A.W., McMahon, K.L., de Zubicaray, G.I., Martin, N.G., Wright, M.J., Thompson, P.M., 2012. Test-retest reliability of graph theory measures of structural brain connectivity. In: Ayache, N., Delingette, H., Golland, P., Mori, K. (Eds.), Medical Image Computing and Computer-Assisted Intervention – MICCAI 2012. Springer Berlin Heidelberg, Berlin, Heidelberg, pp. 305–312. doi:10.1007/978-3-642-33454-2_38.

Desikan, R.S., Ségonne, F., Fischl, B., Quinn, B.T., Dickerson, B.C., Blacker, D., Buckner, R.L., Dale, A.M., Maguire, R.P., Hyman, B.T., Albert, M.S., Killiany, R.J., 2006. An automated labeling system for subdividing the human cerebral cortex on mri scans into gyral based regions of interest. Neuroimage 31 (3), 968–980. doi:10.1016/j.neuroimage.2006.01.021.

Endo, H., Hiroe, N., Yamashita, O., 2020. Evaluation of resting spatio-temporal dynamics of a neural mass model using resting fmri connectivity and EEG microstates. Front. Comput. Neurosci. 13. doi:10.3389/fncom.2019.00091.

Freeman, W.J., 1987. Simulation of chaotic EEG patterns with a dynamic model of the olfactory system. Biol. Cybern. 56 (2–3), 139–150. doi:10.1007/bf00317988.

Fukushima, M., Sporns, O., 2018. Comparison of fluctuations in global network topology of modeled and empirical brain functional connectivity. PLoS Comput. Biol. 14 (9), e1006497. doi:10.1371/journal.pcbi.1006497.

Goñi, J., van den Heuvel, M.P., Avena-Koenigsberger, A., Velez de Mendizabal, N., Betzel, R.F., Griffa, A., Hagmann, P., Corominas-Murtra, B., Thiran, J.-P., Sporns, O., 2014. Resting-brain functional connectivity predicted by analytic measures of network communication. PNAS; Proceedings of the National Academy of Sciences 111 (2), 833. doi:10.1073/pnas.1315529111.

Griffanti, L., Salimi-Khorshidi, G., Beckmann, C.F., Auerbach, E.J., Douaud, G., Sexton, C.E., Zsoldos, E., Ebmeier, K.P., Filippini, N., Mackay, C.E., Moeller, S., Xu, J., Yacoub, E., Baselli, G., Ugurbil, K., Miller, K.L., Smith, S.M., 2014. Ica-based artefact removal and accelerated fmri acquisition for improved resting state network imaging. Neuroimage 95, 232–247. doi:10.1016/j.neuroimage.2014.03.034.

Hagmann, P., Cammoun, L., Gigandet, X., Meuli, R., Honey, C.J., Wedeen, V.J., Sporns, O., 2008. Mapping the structural core of human cerebral cortex. PLoS Biol. 6 (7), e159. doi:10.1371/journal.pbio.0060159.

van den Heuvel, M.P., Sporns, O., 2011. Rich-club organization of the human connectome. J. Neurosci. 31 (44), 15775–15786. doi:10.1523/JNEUROSCI.3539-11.2011.

Hodgkin, A.L., Huxley, A.F., 1952. A quantitative description of membrane current and its application to conduction and excitation in nerve. J. Physiol. (Lond.) 117 (4), 500–544. doi:10.1113/jphysiol.1952.sp004764.

Honey, C., Sporns, O., Cammoun, L., Gigandet, X., Thiran, J., Meuli, R., Hagmann, P., 2009. Predicting human resting-state functional connectivity from structural connectivity. PNAS; Proceedings of the National Academy of Sciences 106 (6), 2035–2040. doi:10.1073/pnas.0811168106.

Jansen, B.H., Rit, V.G., 1995. Electroencephalogram and visual evoked potential generation in a mathematical model of coupled cortical columns. Biol. Cybern. 73 (4), 357–366. doi:10.1007/bf00199471.

Jeurissen, B., Tournier, J.-D., Dhollander, T., Connelly, A., Sijbers, J., 2014. Multi-tissue constrained spherical deconvolution for improved analysis of multi-shell diffusion mri data. Neuroimage 103, 411–426. doi:10.1016/j.neuroimage.2014.07.061.

Jones, D.K., Knösche, T.R., Turner, R., 2013. White matter integrity, fiber count, and other fallacies: the do's and don'ts of diffusion mri. Neuroimage 73, 239–254. doi:10.1016/j.neuroimage.2012.06.081.

Jülich Supercomputing Centre, 2018. JURECA: Modular supercomputer at jülich supercomputing centre. Journal of large-scale research facilities 4 (A132). doi:10.17815/jlsrf-4-121-1.

Knock, S.A., McIntosh, A.R., Sporns, O., Kotter, R., Hagmann, P., Jirsa, V.K., 2009. The effects of physiologically plausible connectivity structure on local and global dynamics in large scale brain models. J. Neurosci. Methods 183, 86–94. doi:10.1016/j.jneumeth.2009.07.007.

Kuramoto, Y., 1984. Chemical oscillations, waves, and turbulence. Springer Berlin Heidelberg doi:10.1007/978-3-642-69689-3.

Lindquist, M., 2020. Neuroimaging results altered by varying analysis pipelines. Nature 582 (7810), 36–37. doi:10.1038/d41586-020-01282-z.

Maier-Hein, K.H., Neher, P.F., Houde, J.-C., Côté, M.-A., Garyfallidis, E., Zhong, J., Chamberland, M., Yeh, F.-C., Lin, Y.-C., Ji, Q., Reddick, W.E., Glass, J.O., Chen, D.Q., Feng, Y., Gao, C., Wu, Y., Ma, J., He, R., Li, Q., Westin, C.-F., Deslauriers-Gauthier, S., González, J.O.O., Paquette, M., St-Jean, S., Girard, G., Rheault, F., Sidhu, J., Tax, C.M.W., Guo, F., Mesri, H.Y., Dávid, S., Froeling, M., Heemskerk, A.M., Leemans, A., Boré, A., Pinsard, B., Bedetti, C., Desrosiers, M., Brambati, S., Doyon, J., Sarica, A., Vasta, R., Cerasa, A., Quattrone, A., Yeatman, J., Khan, A.R., Hodges, W., Alexander, S., Romascano, D., Barakovic, M., Auría, A., Esteban, O., Lemkaddem, A., Thiran, J.-P., Cetingul, H.E., Odry, B.L., Mailhe, B., Nadar, M.S., Pizzagalli, F., Prasad, G., Villalon-Reina, J.E., Galvis, J., Thompson, P.M., Requejo, F.D.S., Laguna, P.L., Lacerda, L.M., Barrett, R., Dell'Acqua, F., Catani, M., Petit, L., Caruyer, E., Daducci, A., Dyrby, T.B., Holland-Letz, T., Hilgetag, C.C., Stieltjes, B., Descoteaux, M., 2017. The challenge of mapping the human connectome based on diffusion tractography. Nat. Commun. 8 (1). doi:10.1038/s41467-017-01285-x.

Messaritaki, E., Dimitriadis, S.I., Jones, D.K., 2019. Optimization of graph construction can significantly increase the power of structural brain network studies. Neuroimage 199, 495–511. doi:10.1016/j.neuroimage.2019.05.052.

Owen, J.P., Ziv, E., Bukshpun, P., Pojman, N., Wakahiro, M., Berman, J.I., Roberts, T.P., Friedman, E.J., Sherr, E.H., Mukherjee, P., 2013. Test–retest reliability of computational network measurements derived from the structural connectome of the human brain. Brain Connect. 3 (2), 160–176. doi:10.1089/brain.2012.0121.

Parkes, L., Fulcher, B., Yücel, M., Fornito, A., 2018. An evaluation of the efficacy, reliability, and sensitivity of motion correction strategies for resting-state functional mri. Neuroimage 171, 415–436. doi:10.1016/j.neuroimage.2017.12.073.

Ponce-Alvarez, A., Deco, G., Hagmann, P., Romani, G.L., Mantini, D., Corbetta, M., 2015. Resting-state temporal synchronization networks emerge from connectivity topology and heterogeneity. PLoS Comput. Biol. 11 (2), e1004100. doi:10.1371/journal.pcbi.1004100.

Popovych, O.V., Manos, T., Hoffstaedter, F., Eickhoff, S.B., 2019. What can computational models contribute to neuroimaging data analytics? Front. Syst. Neurosci. 12. doi:10.3389/fnsys.2018.00068.

Popovych, O.V., Yanchuk, S., Tass, P.A., 2011. Delay- and coupling-induced firing patterns in oscillatory neural loops. Phys. Rev. Lett. 107, 228102. doi:10.1103/PhysRevLett.107.228102.

Prasad, G., Nir, T.M., Toga, A.W., Thompson, P.M., 2013. Tractography density and network measures in alzheimer's disease. In: 2013 IEEE 10th International Symposium on Biomedical Imaging, pp. 692–695. doi:10.1109/ISBI.2013.6556569.

Proix, T., Spiegler, A., Schirner, M., Rothmeier, S., Ritter, P., Jirsa, V.K., 2016. How do parcellation size and short-range connectivity affect dynamics in large-scale brain network models? Neuroimage 142, 135–149. doi:10.1016/j.neuroimage.2016.06.016.

Qi, S., Meesters, S., Nicolay, K., ter Haar Romeny, B.M., Ossenblok, P., 2015. The influence of construction methodology on structural brain network measures: a review. J. Neurosci. Methods 253, 170–182. doi:10.1016/j.jneumeth.2015.06.016.

Rodrigues, F.A., Peron, T.K.D., Ji, P., Kurths, J., 2016. The kuramoto model in complex networks. Phys Rep 610, 1–98. doi:10.1016/j.physrep.2015.10.008.

Roine, T., Jeurissen, B., Perrone, D., Aelterman, J., Philips, W., Sijbers, J., Leemans, A., 2019. Reproducibility and intercorrelation of graph theoretical measures in structural brain connectivity networks. Med. Image Anal. 52, 56–67. doi:10.1016/j.media.2018.10.009.

Rubinov, M., Sporns, O., 2010. Complex network measures of brain connectivity: uses and interpretations. Neuroimage 52 (3), 1059–1069. doi:10.1016/j.neuroimage.2009.10.003.

Schaefer, A., Kong, R., Gordon, E.M., Laumann, T.O., Zuo, X.-N., Holmes, A.J., Eickhoff, S.B., Yeo, B.T.T., 2018. Local-Global parcellation of the human cerebral cortex from intrinsic functional connectivity MRI. Cerebral Cortex 28 (9), 3095–3114. doi:10.1093/cercor/bhx179.

Schilling, K.G., Nath, V., Hansen, C., Parvathaneni, P., Blaber, J., Gao, Y., Neher, P., Aydogan, D.B., Shi, Y., Ocampo-Pineda, M., Schiavi, S., Daducci, A., Girard, G., Barakovic, M., Rafael-Patino, J., Romascano, D., Rensonnet, G., Pizzolato, M., Bates, A., Fischi, E., Thiran, J.-P., Canales-Rodríguez, E.J., Huang, C., Zhu, H., Zhong, L., Cabeen, R., Toga, A.W., Rheault, F., Theaud, G., Houde, J.-C., Sidhu, J., Chamberland, M., Westin, C.-F., Dyrby, T.B., Verma, R., Rathi, Y., Irfanoglu, M.O., Thomas, C., Pierpaoli, C., Descoteaux, M., Anderson, A.W., Landman, B.A., 2019. Limits to anatomical accuracy of diffusion tractography using modern approaches. Neuroimage 185, 1–11. doi:10.1016/j.neuroimage.2018.10.029.

Smith, S.M., Beckmann, C.F., Andersson, J., Auerbach, E.J., Bijsterbosch, J., Douaud, G., Duff, E., Feinberg, D.A., Griffanti, L., Harms, M.P., Kelly, M., Laumann, T., Miller, K.L., Moeller, S., Petersen, S., Power, J., Salimi-Khorshidi, G., Snyder, A.Z., Vu, A.T., Woolrich, M.W., Xu, J., Yacoub, E., Ugurbil, K., Van Essen, D.C., Glasser, M.F., 2013. Resting-state fmri in the human connectome project. Neuroimage 80, 144–168. doi:10.1016/j.neuroimage.2013.05.039.

Smith, S.M., Jenkinson, M., Woolrich, M.W., Beckmann, C.F., Behrens, T.E., Johansen-Berg, H., Bannister, P.R., De Luca, M., Drobnjak, I., Flitney, D.E., Niazy, R.K., Saunders, J., Vickers, J., Zhang, Y., De Stefano, N., Brady, J.M., Matthews, P.M., 2004. Advances in functional and structural mr image analysis and implementation as fsl. Neuroimage 23, S208–S219. doi:10.1016/j.neuroimage.2004.07.051.

Sotiropoulos, S.N., Zalesky, A., 2019. Building connectomes using diffusion mri: why, how and but. NMR Biomed. 32 (4), e3752. doi:10.1002/nbm.3752.

Sporns, O., 2011. The human connectome: a complex network. Ann. N. Y. Acad. Sci. 1224 (1), 109–125. doi:10.1111/j.1749-6632.2010.05888.x.

Sporns, O., Tononi, G., Kötter, R., 2005. The human connectome: a structural description of the human brain. PLoS Comput. Biol. 1 (4). doi:10.1371/journal.pcbi.0010042.

Suárez, L.E., Markello, R.D., Betzel, R.F., Misic, B., 2020. Linking structure and function in macroscale brain networks. Trends Cogn. Sci. (Regul. Ed.) 24 (4), 302–315. doi:10.1016/j.tics.2020.01.008.

Thirion, B., Varoquaux, G., Dohmatob, E., Poline, J.-B., 2014. Which fmri clustering gives good brain parcellations? Front. Neurosci. 8, 167. doi:10.3389/fnins.2014.00167.

Ton, R., Deco, G., Daffertshofer, A., 2014. Structure-function discrepancy: inhomogeneity and delays in synchronized neural networks. PLoS Comput. Biol. 10 (7), e1003736. doi:10.1371/journal.pcbi.1003736.

Tournier, J.D., Calamante, F., Connelly, A., 2010. Improved probabilistic streamlines tractography by 2nd order integration over fibre orientation distributions. In: Proceedings of the international society for magnetic resonance in medicine, 1670. ISMRM.

Tournier, J.-D., Smith, R., Raffelt, D., Tabbara, R., Dhollander, T., Pietsch, M., Christiaens, D., Jeurissen, B., Yeh, C.-H., Connelly, A., 2019. Mrtrix3: a fast, flexible and open software framework for medical image processing and visualisation. Neuroimage 202, 116137. doi:10.1016/j.neuroimage.2019.116137.

Tustison, N.J., Avants, B.B., Cook, P.A., Zheng, Y., Egan, A., Yushkevich, P.A., Gee, J.C., 2010. N4itk: Improved n3 bias correction. IEEE Trans. Med. Imaging 29 (6), 1310–1320. doi:10.1109/TMI.2010.2046908.

Van Essen, D.C., Smith, S.M., Barch, D.M., Behrens, T.E., Yacoub, E., Ugurbil, K., 2013. The wu-minn human connectome project: an overview. Neuroimage 80, 62–79. doi:10.1016/j.neuroimage.2013.05.041.

Vergani, F., Lacerda, L., Martino, J., Attems, J., Morris, C., Mitchell, P., de Schotten, M.T., Dell'Acqua, F., 2014. White matter connections of the supplementary motor area in humans. Journal of Neurology, Neurosurgery & Psychiatry 85 (12), 1377–1385. doi:10.1136/jnnp-2013-307492.

Wilson, H.R., Cowan, J.D., 1973. A mathematical theory of the functional dynamics of cortical and thalamic nervous tissue. Kybernetik 13 (2), 55–80. doi:10.1007/bf00288786.

Yeung, M.K.S., Strogatz, S.H., 1999. Time delay in the kuramoto model of coupled oscillators. Phys. Rev. Lett. 82, 648–651. doi:10.1103/PhysRevLett.82.648.

Zimmermann, J., Perry, A., Breakspear, M., Schirner, M., Sachdev, P., Wen, W., Kochan, N., Mapstone, M., Ritter, P., McIntosh, A., Solodkin, A., 2018. Differentiation of alzheimer's disease based on local and global parameters in personalized virtual brain models. NeuroImage: Clinical 19, 240–251. doi:10.1016/j.nicl.2018.04.017.